



Physical Properties of the Host Galaxies of Ca-rich Transients

Yuxin Dong (董雨欣)^{1,2} , Dan Milisavljevic^{1,3} , Joel Leja^{4,5,6} , Sumit K. Sarbadhickey^{7,8} , Anya E. Nugent² ,
Raffaella Margutti⁹ , Wynn V. Jacobson-Galán⁹ , Abigail Polin^{10,11} , John Banovetz¹ , Jack M. Reynolds¹, and
Bhagya Subrayan¹ 

¹ Department of Physics and Astronomy, Purdue University, 525 Northwestern Avenue, West Lafayette, IN 47907, USA

² Center for Interdisciplinary Exploration and Research in Astrophysics (CIERA) and Department of Physics and Astronomy, Northwestern University, Evanston, IL 60208, USA

³ Integrative Data Science Initiative, Purdue University, West Lafayette, IN 47907, USA

⁴ Department of Astronomy & Astrophysics, The Pennsylvania State University, University Park, PA 16802, USA

⁵ Institute for Computational & Data Sciences, The Pennsylvania State University, University Park, PA, USA

⁶ Institute for Gravitation and the Cosmos, The Pennsylvania State University, University Park, PA 16802, USA

⁷ Department of Astronomy and Astrophysics, Michigan State University, 567 Wilson Road, East Lansing, MI 48824, USA

⁸ Center for Cosmology and AstroParticle Physics (CCAPP), The Ohio State University, 191 West Woodruff Avenue, Columbus, OH 43210, USA

⁹ Department of Astronomy, University of California, Berkeley, CA 94720-3411, USA

¹⁰ The Observatories of the Carnegie Institution for Science, 813 Santa Barbara Street, Pasadena, CA 91101, USA

¹¹ TAPIR, Walter Burke Institute for Theoretical Physics, 350-17, Caltech, Pasadena, CA 91125, USA

Received 2021 September 20; revised 2022 February 3; accepted 2022 February 4; published 2022 March 17

Abstract

Calcium-rich (Ca-rich) transients are a new class of supernovae (SNe) that are known for their comparatively rapid evolution, modest peak luminosities, and strong nebular calcium emission lines. Currently, the progenitor systems of Ca-rich transients remain unknown. Although they exhibit spectroscopic properties not unlike core-collapse Type Ib/c SNe, nearly half are found in the outskirts of their host galaxies, which are predominantly elliptical, suggesting a closer connection to the older stellar populations of SNe Ia. In this paper, we present a compilation of publicly available multiwavelength observations of all known and/or suspected host galaxies of Ca-rich transients ranging from far-UV to IR, and use these data to characterize their stellar populations with PROSPECTOR. We estimate several galaxy parameters including integrated star formation rate, stellar mass, metallicity, and age. For nine host galaxies, the observations are sensitive enough to obtain nonparametric star formation histories, from which we recover SN rates and estimate probabilities that the Ca-rich transients in each of these host galaxies originated from a core-collapse versus Type Ia-like explosion. Our work supports the notion that the population of Ca-rich transients do not come exclusively from core-collapse explosions, and must either be only from white dwarf stars or a mixed population of white dwarf stars with other channels, potentially including massive star explosions. Additional photometry and explosion site spectroscopy of larger samples of Ca-rich host galaxies will improve these estimates and better constrain the ratio of white dwarf versus massive star progenitors of Ca-rich transients.

Unified Astronomy Thesaurus concepts: [Supernovae \(1668\)](#); [Galaxies \(573\)](#); [Photometry \(1234\)](#)

1. Introduction

Understanding the progenitor systems of Calcium-rich (Ca-rich) transients is an active research topic in time-domain astrophysics. Compared to Type Ia and core-collapse (Type II, IIb, Ib/c) supernovae (SNe), Ca-rich transients evolve more rapidly into the nebular phase of emission (Kasliwal et al. 2012). At early epochs, their spectra strongly resemble those of stripped-envelope Type Ib/c SNe, showing prominent lines of He I, O I, Mg II, and Ca II with large photospheric velocities ($\approx 11,000$ km s⁻¹; Perets et al. 2010; Kasliwal et al. 2012; Taubenberger 2017). At later nebular epochs, they become *rich* in [Ca II] $\lambda\lambda 7291, 7324$ emission lines with an integrated [Ca II]/[O I] $\lambda\lambda 6300, 6364$ flux ratio $\gtrsim 2$ (Milisavljevic et al. 2017; Jacobson-Galán et al. 2020a).

Although Ca-rich transients may make up only a small fraction of all SN events (10%–20% of SNe Ia; De et al. 2020, but see also Frohmaier et al. 2018), knowing their origin is

nevertheless critical in understanding their role in chemical enrichment of the universe. Ca-rich transients may produce large amounts of calcium ($\sim 0.1 M_{\odot}$; Perets et al. 2010), and in turn may be significant contributors to the calcium content of the intracluster medium (Mulchaey et al. 2014). However, more recent theoretical investigations (Dessart & Hillier 2015; Jacobson-Galán et al. 2020a; Polin et al. 2021), and analyses leveraging optical+near-infrared observations (Milisavljevic et al. 2017), have instead supported the notion that these explosions are far less abundant in calcium production than originally suspected (0.006 – $0.02 M_{\odot}$).

Many progenitor models have been suggested to explain the origin of Ca-rich transients. Ca-rich transients are often located at large offset distances away from their suspected host galaxies ($\sim 1/3$ are offset >20 kpc; Kasliwal et al. 2012; Foley 2015; Lyman et al. 2016), and nearly half are discovered in older galaxies that exhibit sparse star formation, which together suggest a connection with white dwarf (WD) stars and an explosion potentially triggered by a helium detonation process (Bildsten et al. 2007; Shen & Bildsten 2009; Perets et al. 2010; Woosley & Kasen 2011). However, the spectroscopic similarities between a large fraction of Ca-rich transients and core-collapse SNe which are found in galaxies with ongoing star formation,



Original content from this work may be used under the terms of the [Creative Commons Attribution 4.0 licence](#). Any further distribution of this work must maintain attribution to the author(s) and the title of the work, journal citation and DOI.

instead suggest connections with massive stars (Kawabata et al. 2010; Milisavljevic et al. 2017; Lee et al. 2019). Binary evolution involving a low-mass He or C/O progenitor star with a neutron star companion producing an *ultra-stripped* SN has also been suggested (Tauris et al. 2015), as have mergers between neutron stars and WDs (Metzger 2012; Lyman et al. 2014), and the tidal detonation of a WD by a neutron star or black hole (Rosswog et al. 2008; Clausen & Eracleous 2011; Metzger 2012; MacLeod et al. 2014; Sell et al. 2015; Margalit & Metzger 2016; Bobrick et al. 2017; Zenati et al. 2019).

Recently, De et al. (2020) distinguished Ca-rich transients into Ca Ib/c and Ca Ia subclasses by features observed in photospheric phase spectra that are similar to Type Ia and Ib/c SNe, respectively. In this system, Ca Ia objects are believed to be a complete double detonation of low-mass WDs where the efficiency of He burning in the outer ejecta is high, whereas Ca Ib/c objects are produced from a continuum of double detonations on even lower mass WDs (Ca-Ic) to He shell-only detonations or deflagrations (Ca Ib) all with low He burning efficiency.

The possibility that multiple progenitor channels contribute to the observed diversity of Ca-rich transients has not yet been ruled out, and the debated nature of many well-observed Ca-rich transients continues to fuel this uncertainty. Most recently, multiple progenitor scenarios have been suggested for SN2019ehk in NGC 4321 (M100), the first and only Ca-rich transient with X-ray detections: an ultra-stripped SN (Nakaoka et al. 2021), a helium shell detonation on a sub-Chandrasekhar WD (Jacobson-Galán et al. 2020a, 2021), interaction of lowest mass massive star (9.5–10 M_{\odot}) binaries (Jacobson-Galán et al. 2020a), and core collapse from a stripped-envelope massive star (De et al. 2021). Further complicating efforts to unify the class are a variety of objects with properties that bridge classifications. For example, the peculiar iPTF15eqv was more luminous and decayed much more slowly than other Ca-rich transients, but had one of the highest [Ca II]/[O I] flux ratios among all Ca-rich transients (Milisavljevic et al. 2017).

To date, there has been considerable effort to constrain potential progenitor systems of Ca-rich transients using host galaxy information (see, e.g., Yuan et al. 2013; Lunnan et al. 2017; Shen et al. 2019; Perets & Beniamini 2021). Here, we further these efforts by presenting a comprehensive analysis of the host galaxies of all reported and suspected Ca-rich transients using publicly available photometry and the parametric and nonparametric models in the advanced stellar inference Python package PROSPECTOR (Leja et al. 2017; Johnson et al. 2021). We examine the properties of these host galaxies, including star formation, age, mass, and metallicity, to further constrain the potential progenitor systems of Ca-rich transients. The layout of the paper is structured with the following sections. Section 2 includes the various catalogs and bands used to create our data sets. Section 3 describes the spectral energy distribution (SED) modeling using PROSPECTOR. The results from using the parametric and nonparametric models are in Section 4. Section 5 discusses and summarizes the interpretation and comparisons between our results in the two models.

2. Observations

The 19 Ca-rich transients and their associated host galaxies found in the literature and used in this paper are listed in Table 1. Images are shown in Figures 1–3. The host morphology is determined according to classifications given by de Vaucouleurs et al. (1964). We utilize broadband photometry from the $z=0$

Table 1
Ca-rich Transient Samples & Host Galaxies

SN	Host Galaxy	Host Type	Host Redshift	Reference
2000ds	NGC 2768	E6	0.00451	6
2001co	NGC 5559	SBb	0.01723	6
2003H	NGC 2207	SABb/c	0.00914	6
2003dg	UGC 6934	SAC/d	0.01835	6
2003dr	NGC 5714	Scd	0.00746	4, 6
2005E	NGC 1032	S0/A	0.00899	1, 6
2005cz	NGC 4589	E2	0.00660	2, 6
2007ke	NGC 1129	E0	0.01733	6
2010et	CGCG 170-011	E0	0.02334	6
2012hn	NGC 2272	E	0.00710	5, 6
2016hmk	MCG-01-06-070	SAB	0.01627	10, 11, 13
2019ehk	NGC 4321	SAB(s)bc	0.00524	12, 14, 15
PTF09dav	2MASX J22465295 +2138221	S (Disturbed)	0.03710	6, 3
PTF10hew	NGC 2639	SAa	0.01113	8
PTF11bij	IC 3956	E3	0.03471	4, 6
PTF11kmb	NGC 7265	S	0.01696	8
PTF12bho	WISEA J130109.43 +280159.1	E	0.02339	8
iPTF15eqv	NGC 3430	SAB	0.00529	7
iPTF16hgs	2MASX J00505254 +2722432	S	0.01700	9

Note. Information on the Ca-rich samples included in this work and their putative host galaxies. All redshifts are from NED with the exception of the host of iPTF16hgs which comes from De et al. (2018). Classifications of host galaxies are also from NED (de Vaucouleurs et al. 1964).

References: (1) Perets et al. (2010), (2) Kawabata et al. (2010), (3) Sullivan et al. (2011), (4) Kasliwal et al. (2012), (5) Valenti et al. (2014), (6) Foley (2015), (7) Milisavljevic et al. (2017), (8) Lunnan et al. (2017), (9) De et al. (2018), (10) Sell et al. (2018), (11) Galbany et al. (2019), (12) Jacobson-Galán et al. (2020a), (13) Jacobson-Galán et al. (2020b), (14) De et al. (2021), (15) Jacobson-Galán et al. (2021).

Multiwavelength Galaxy Synthesis I (z0MGS; Leroy et al. 2019), which is an atlas that contains ultraviolet (UV) and infrared (IR) images as observed by the Galaxy Evolution Explorer (GALEX; Martin et al. 2005) and Wide-field Infrared Survey Explorer (WISE; Wright et al. 2010) surveys. The atlas selects a sample of local galaxies ($d \lesssim 50$ Mpc) from the Lyon Extragalactic Database (LEDA; Paturel et al. 2003b; Makarov et al. 2014a) and measures integrated-light photometry in far-UV (FUV), near-UV (NUV), W1, W2, W3, and W4 bands. The maps contain matched resolution and astrometry to ensure consistency across all resolved measurements.

We supplement these data with photometry from a variety of catalogs. Additional optical data are retrieved from the Sloan Digital Sky Survey Data Release 13 (SDSS DR13; Albareti et al. 2017). SDSS DR13 includes all coverage of prior data releases in the northern hemisphere and recalibrations of SDSS imaging catalogs. We correct for Galactic dust extinction for the optical photometry using Galactic reddening maps from Schlegel et al. (1998) and NASA/IPAC Extragalactic Database (NED).¹² IR photometry in the J -, H -, and K -bands are extracted from the Two Micron All Sky Survey All-Sky

¹² <https://ned.ipac.caltech.edu/>

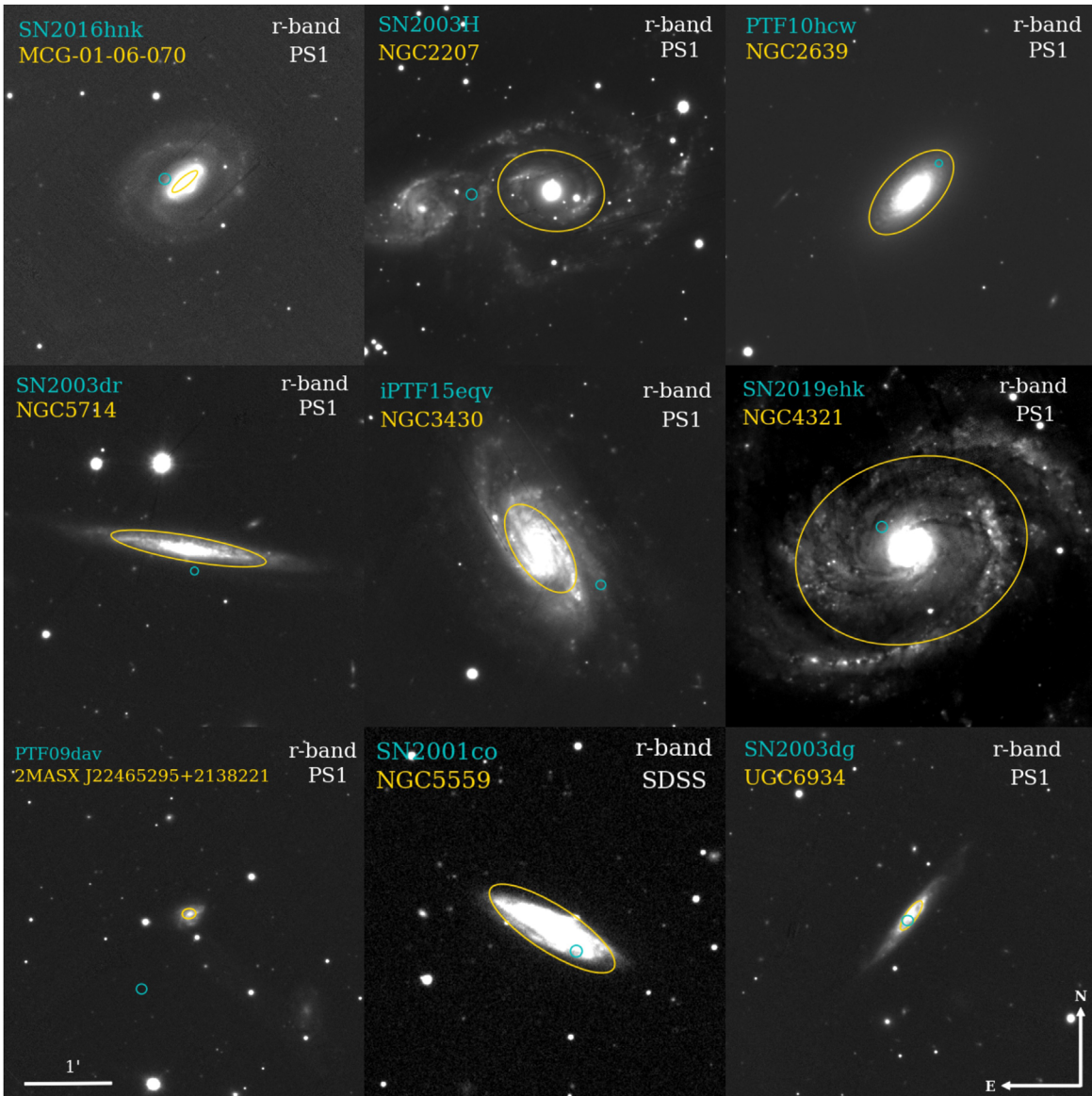


Figure 1. Spiral host galaxies in our sample as observed by Pan-STARRS and SDSS. Each panel is 4×4 arcmin² and aligned north up and east left with the same scale. The name of the SN and host galaxy are indicated on the top left hand corner while the filter and survey are displayed on the top right hand corner. All host galaxies are circled in yellow and transients in blue. The ellipses are at twice the isophotal radius.

(2MASS) Extended Source Catalog (Skrutskie et al. 2006) in the NASA/IPAC Infrared Science Archive (Skrutskie et al. 2006) and the 2MASS Large Galaxy Atlas (Jarrett et al. 2003) cataloged by Bai et al. (2015).

Photometry in g , r , and z are included from the Legacy Surveys Data Release 8 (DR8), as well as mid-IR photometry in the 3.4 and 4.6 μm WISE bands from the DESI Legacy Imaging Surveys (Dey et al. 2019). While both the DESI survey and the z0MGS atlas employ data from the WISE mission, the former targets the two shortest-wavelengths, W1 and W2, and measures the photometry using *The Tractor* algorithms (Lang et al. 2016) while the latter contains all four WISE bands directly from imaging. All photometry measurements in DESI are aperture-matched using *The Tractor* package.

We also incorporate optical photometry from Pan-STARRS Data Release 2 (PS2; Flewelling 2018) and HyperLeda (Paturel et al. 2003a; Makarov et al. 2014b) compiled by Bai et al. (2015) for galaxies that do not have any optical photometry from SDSS

DR13 or DESI DR8. Using the equations and coefficients from Tonry et al. (2012), we transform g , r , i , and z magnitudes in PS2 to SDSS bandpasses and keep the y band as is. Since photometry from DESI and PS2 are not extinction corrected, we perform the same Galactic dust extinction correction as before. For uniformity and consistency in the data, we convert all broadband photometry to AB magnitudes. In the case of three host galaxies, NGC 2207, UGC 6934, and MCG-01-06-070, photometry from 2MASS and DESI were inconsistent across other surveys, and were excluded from our fits. The mismatch is most likely the result of inconsistent aperture extraction and/or poorly determined zero-points. The complete photometric data utilized in our models are presented in the Appendix.

SED modeling relies heavily on the quality and completeness of photometry, and our host galaxy samples have a nonuniform number of data points. Johnson et al. (2021) demonstrated that for a small number of photometric bands, the posteriors are largely determined by the prior distributions. Nevertheless, the

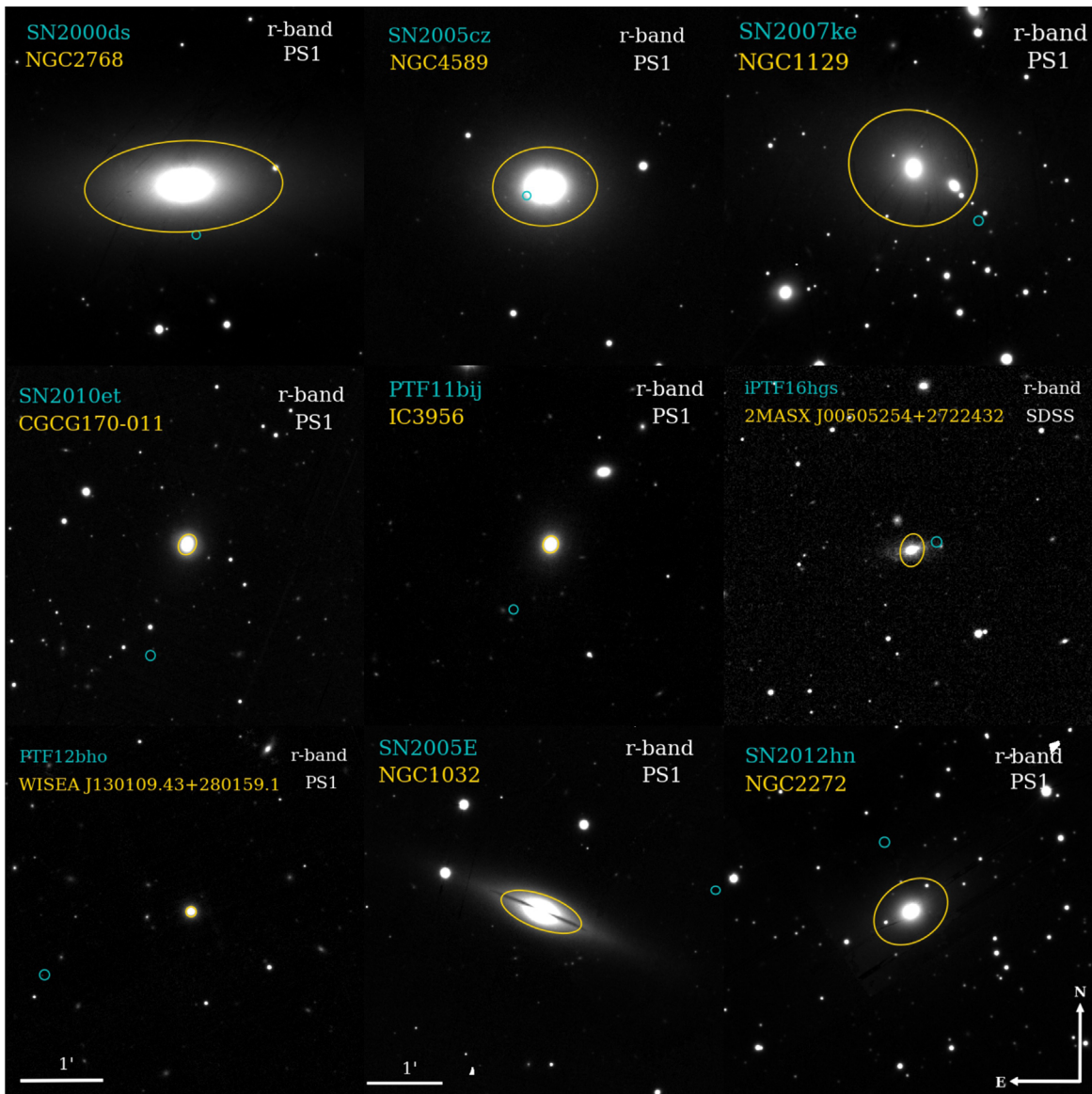


Figure 2. Same as Figure 1, but for all elliptical host galaxies in our sample. Each panel is 4×4 arcmin². This collage also includes NGC 1032, an S0/A type galaxy with a panel size of 5×5 arcmin².

addition of even a single data point can be informative given a reasonable choice of priors and Bayesian reasoning in high-dimension parameter spaces. An increase in the number of photometry bands will only allow the constraints on each parameter to become stronger and distinct from the prior distributions. In light of this, all photometric values are utilized in the SED modeling despite the unevenness of the data sets.

3. SED Modeling

We model host galaxy SEDs with PROSPECTOR, which is an advanced Python package that infers stellar population properties conditioned on the available photometric data (Leja et al. 2017; Johnson et al. 2021). We choose PROSPECTOR as opposed to other similar implementations such as MAGPHYS (da Cunha et al. 2008) and CIGALE (Boquien et al. 2019) to take advantage of its larger, more flexible parameter space. PROSPECTOR also allows users to specify their priors on-the-fly and examine the resulting effect on their posteriors. Further, PROSPECTOR fits the observational data using *dynesty* (Speagle 2020), a dynamic

nested sampling method that is more efficient than the traditional Markov Chain Monte Carlo approach. Besides the spectroscopic redshift for the host of iPTF16hgs from De et al. (2018), heliocentric redshift is adopted from NED in all photometric fits. For photometry with small observational uncertainties, a 5% error floor is put in place. This is to account for systematic model uncertainties as stellar population models are products of an amalgamation of theory, empirical libraries, and occasionally, ad hoc assumptions (Conroy et al. 2009; Conroy 2013; Leja et al. 2019b; Alsing et al. 2020).

To build the stellar population models, PROSPECTOR utilizes the Flexible Stellar Populations Synthesis (FSPS) code (Conroy et al. 2009; Conroy & Gunn 2010) and *Python-fsps* (Foreman-Mackey et al. 2014) for Python interface. It also uses Wilkinson Microwave Anisotropy Probe 9 cosmology (Hinshaw et al. 2013) internally. For our work, we employ both a parametric and a more sophisticated nonparametric *continuity sfh* model to compare the results under different assumptions in each respective model.

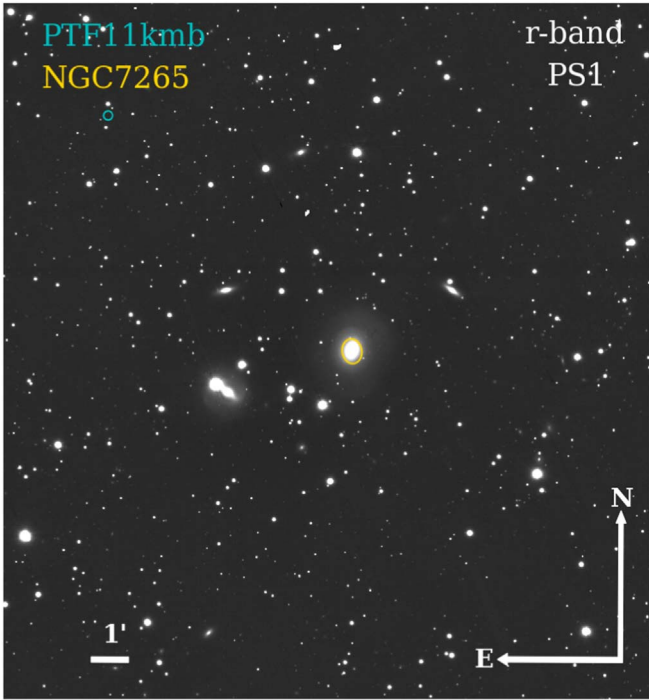


Figure 3. Same as Figures 1 and 2, but for the suspected host galaxy of PTF11kmb. The panel is 15×15 arcmin².

We use standard GALEX, Bessell, SDSS, Pan-STARRS, 2MASS, and WISE transmission curves in our photometry data that are fitted in the SED modeling. For consistency and a reasonable comparison, we also employ a Chabrier initial mass function (IMF; Chabrier 2003) and Milky Way extinction law (Cardelli et al. 1989) in both models.

Dust plays a critical role in nearly all galaxies as it obscures light in the UV and emits it in the IR wavelengths (Conroy 2013). In particular, dust emission from dust grains dominates the SED redward of $>3 \mu\text{m}$. The dust grains are postulated to be polycyclic aromatic hydrocarbon (PAH) particles as mixtures of amorphous silicate and graphite (Draine & Li 2007). Thus, for any hosts that have photometry $>3 \mu\text{m}$ (i.e., WISE bands), we implement the dust emission model from Draine & Li (2007) to describe the PAH thermal emission features. The model is parameterized by the mass fraction of dust in PAH form, q_{PAH} , the minimum radiation strength U_{min} , and the fraction γ of dust in high radiation fields. These metrics are set as free parameters in both models to allow for more accurate uncertainties in the posterior distributions.

In both models, we incorporate nebular continuum in our model spectra and impose a 2:1 ratio on the amount of dust attenuation between the young and old stellar populations for the star-forming galaxies as younger stars tend to attenuate roughly twice the amount of dust in star-forming regions as older stars (Calzetti et al. 2000). The stellar mass—stellar metallicity ($M_* - Z$) relationship from Gallazzi et al. (2005) is implemented as a prior for all host samples at their respective redshifts, following the implementation in Leja et al. (2017) where the width of the relationship is doubled to account for potential systemic errors.

3.1. Parametric Model

In our analyses, we first use a parametric model that is built with five unbiased free parameters: total mass in stars and remnants (M), metallicity (Z), star formation timescale (τ),

lookback time at which star formation commences (t_{age}), and dust extinction (A_V). In this model, the star formation history (SFH) is parameterized by the delayed- τ function form from Simha et al. (2014). Moreover, the star formation rate (SFR) is given by

$$\text{SFR}(t) = M \times \left[\int_0^t t' e^{-t'/\tau} dt' \right]^{-1} \times t e^{-t/\tau},$$

where τ is a free parameter that describes a star formation timescale for the exponentially declining SFH, M is the total mass formed, and $t = t_{\text{age}}$ (Nugent et al. 2020).

We use t_{age} and τ to calculate t_m , the mass-weighted age through

$$t_m = t_{\text{age}} - \frac{\int_0^{t_{\text{age}}} t \times \text{SFR}(t) dt}{\int_0^{t_{\text{age}}} \text{SFR}(t) dt}$$

(Nugent et al. 2020) to compare ages in our samples. This is a more robust metric of age than t_{age} , which only describes the start of star formation and provides a better estimate compared to light-weighted age since it does not overweigh the light from brighter and younger stars. The mass from the parametric fits denotes the total mass formed in the galaxies that includes the effects of stellar mass through stellar evolution such as SNe and asymptotic giant branch star winds. We convert total mass to stellar mass using t_m and M at the time of the observation. We will only quote mass-weighted ages (t_m) and stellar masses (M_*) hereafter.

3.2. Nonparametric Continuity Model

The `continuity_sfh` model is one of five nonparametric priors available in PROSPECTOR. In the parametric model, the SFH is constrained to a rigid function form; the nonparametric models are developed to allow for extra flexibility in SFHs that the parametric model is not attuned for. Specifically, `continuity_sfh` model emphasizes a smooth SFH that is more sensitive to recent star bursts than the parametric model (Leja et al. 2019a) and offers a less biased reconstruction of the SFH solely based on the SED (Conroy 2013).

For this model, we adopt a simple stellar population (SSP) to describe the SED temporal evolution of the stellar populations with a total of four parameters: metallicity (Z), dust (A_V), total mass formed (M), and SFR ratios between adjacent age bins. The total mass is split into N bins of equal mass m . We calculate a mass-weighted age for our samples using the following equation:

$$t_m = \frac{\sum_{n=1}^N m_n \times \text{age}_n}{m_{\text{total}}},$$

where m_n is the mass formed in each bin, age_n is the average age in each bin, and m_{total} is the sum of masses in all age bins. We also convert the total mass formed to stellar mass (M_*) using the same method as the parametric model and will refer to t_m and M_* for the rest of the paper.

The continuity prior fits for $\Delta \log(\text{SFR})$ between adjacent age bins with $(N - 1)$ SFH variable. We use eight bins for this analysis as results show that SED fits become largely insensitive to the number of temporal bins as long they surpass four bins (Leja et al. 2019a). The first two bins are fixed at

Table 2
Host Galaxies' Stellar Population Properties for the Parametric Model

Transient	t_m Gyr	$\log(Z/Z_\odot)$	$\log(M_*/M_\odot)$	τ	A_V mag	SFR _{SED} $M_\odot \text{ yr}^{-1}$	$\log(\text{sSFR})$ yr^{-1}
SN2000ds	$6.50^{+0.47}_{-0.38}$	-0.09 ± 0.02	10.76 ± 0.02	$0.70^{+0.05}_{-0.04}$	<0.02	0.025 ± 0.001	-12.37 ± 0.03
SN2001co	$5.99^{+0.97}_{-0.11}$	$0.14^{+0.03}_{-0.05}$	10.47 ± 0.05	$3.27^{+1.13}_{-0.87}$	$1.03^{+0.14}_{-0.16}$	$2.68^{+0.83}_{-0.73}$	$-10.04^{+0.16}_{-0.18}$
SN2003H	$3.92^{+1.32}_{-1.39}$	$0.15^{+0.03}_{-0.05}$	$10.81^{+0.07}_{-0.11}$	$5.44^{+2.28}_{-2.20}$	$1.03^{+0.14}_{-0.16}$	$14.97^{+4.78}_{-2.62}$	$-9.94^{+0.24}_{-0.14}$
SN2003dg	$2.27^{+2.13}_{-1.37}$	$-0.22^{+0.21}_{-0.24}$	$9.79^{+0.16}_{-0.19}$	$2.84^{+3.44}_{-1.60}$	$1.26^{+0.38}_{-0.37}$	$2.31^{+2.06}_{-1.15}$	$-9.43^{+0.48}_{-0.45}$
SN2003dr	$7.35^{+0.34}_{-0.49}$	0.18 ± 0.01	$9.90^{+0.02}_{-0.03}$	$3.47^{+0.47}_{-0.30}$	$0.52^{+0.09}_{-0.06}$	$0.49^{+0.10}_{-0.06}$	$-10.21^{+0.10}_{-0.07}$
SN2005E	$6.90^{+2.38}_{-2.45}$	-0.34 ± 0.10	$10.87^{+0.08}_{-0.12}$	$0.80^{+0.37}_{-0.50}$	$0.18^{+0.05}_{-0.06}$	$0.05^{+0.04}_{-0.05}$	$-12.47^{+0.19}_{-1.77}$
SN2005cz	$5.83^{+1.02}_{-0.76}$	$-0.14^{+0.05}_{-0.08}$	$10.72^{+0.05}_{-0.04}$	$0.61^{+0.11}_{-0.09}$	0.03 ± 0.02	$0.021^{+0.002}_{-0.001}$	$-12.40^{+0.05}_{-0.06}$
SN2007ke	$10.37^{+1.56}_{-2.45}$	$-0.09^{+0.13}_{-0.19}$	$11.46^{+0.04}_{-0.05}$	$0.31^{+0.33}_{-0.16}$	0.37 ± 0.02	<0.10	<-12.46
SN2010et	$5.12^{+1.53}_{-1.29}$	$-0.66^{+0.12}_{-0.08}$	$10.30^{+0.07}_{-0.08}$	$0.33^{+0.32}_{-0.17}$	$0.09^{+0.08}_{-0.06}$	<0.56	<-10.55
SN2012hn	$4.69^{+1.02}_{-0.85}$	$-0.21^{+0.09}_{-0.08}$	$10.38^{+0.06}_{-0.05}$	$0.54^{+0.12}_{-0.10}$	0.02 ± 0.01	0.023 ± 0.001	$-12.01^{+0.06}_{-0.07}$
SN2016hmk	$7.94^{+0.25}_{-0.38}$	$0.18^{+0.00}_{-0.01}$	10.42 ± 0.02	$2.90^{+0.22}_{-0.16}$	$0.17^{+0.16}_{-0.04}$	$1.05^{+0.11}_{-0.11}$	$-10.40^{+0.09}_{-0.06}$
SN2019ehk	$0.89^{+0.96}_{-0.30}$	$0.14^{+0.03}_{-0.06}$	$10.54^{+0.06}_{-0.03}$	$0.31^{+1.22}_{-0.14}$	$0.78^{+0.07}_{-0.15}$	$11.76^{+3.56}_{-3.52}$	$-9.48^{+0.10}_{-0.17}$
PTF09dav	$0.01^{+0.01}_{-0.00}$	$0.18^{+0.01}_{-0.02}$	$8.43^{+0.08}_{-0.05}$	$1.21^{+3.80}_{-0.94}$	$1.82^{+0.14}_{-0.10}$	$12.70^{+3.05}_{-2.58}$	$-7.18^{+0.13}_{-0.18}$
PTF10hcw	$3.03^{+0.85}_{-0.52}$	-0.26 ± 0.09	$10.76^{+0.06}_{-0.05}$	$0.49^{+0.14}_{-0.09}$	$0.68^{+0.10}_{-0.15}$	$0.58^{+0.11}_{-0.15}$	$-11.01^{+0.10}_{-0.15}$
PTF11bjj	$5.42^{+3.04}_{-2.47}$	$-0.22^{+0.20}_{-0.23}$	$10.52^{+0.14}_{-0.18}$	$0.58^{+1.23}_{-0.37}$	$0.84^{+0.33}_{-0.30}$	$0.05^{+1.74}_{-0.05}$	$-11.78^{+1.63}_{-7.04}$
PTF11kmb	$0.51^{+0.57}_{-0.20}$	$-0.01^{+0.11}_{-0.26}$	$9.81^{+0.07}_{-0.06}$	$0.35^{+2.07}_{-0.21}$	$2.53^{+0.35}_{-0.94}$	$7.77^{+9.70}_{-7.36}$	$-8.96^{+0.43}_{-1.25}$
PTF12bho	$3.70^{+3.22}_{-2.11}$	$-0.46^{+0.28}_{-0.21}$	$9.22^{+0.17}_{-0.20}$	$0.69^{+2.59}_{-0.48}$	$0.46^{+0.57}_{-0.33}$	$0.04^{+0.36}_{-0.04}$	$-10.69^{+1.18}_{-4.68}$
iPTF15eqv	$6.58^{+0.25}_{-0.37}$	0.18 ± 0.01	9.96 ± 0.02	$4.60^{+0.39}_{-0.42}$	0.26 ± 0.02	0.94 ± 0.05	-9.99 ± 0.04
iPTF16hgs	$0.82^{+1.49}_{-0.52}$	$-0.26^{+0.24}_{-0.35}$	$8.39^{+0.21}_{-0.18}$	$3.17^{+3.87}_{-2.32}$	$1.28^{+0.32}_{-0.44}$	$0.30^{+0.23}_{-0.16}$	$-8.90^{+0.43}_{-0.53}$

Note. Median values of the posterior distributions and 1σ uncertainties determined from the parametric model in PROSPECTOR. All redshifts are heliocentric. We fit for parameters t_{age} , M_* , A_V , τ , and Z , which describe the stellar population properties of all host galaxies. We also derived t_m , SFR_{SED}, and sSFR using equations from Section 3.1, along with 3σ upper limits on A_V for the host of SN2000ds and SFRs for the hosts of SN2007ke and SN2010et.

0–30 and 30–100 Myr with the youngest bin being the smallest to permit a maximally old stellar population (Leja et al. 2019a). The upper limit for the age bins is calculated as the age of the universe at the respective z of each host galaxy. All temporal bins are spaced equally in logarithmic time except the first two and the last bin since the separation is approximately proportional to the distinguishability of SSPs (Ocvirk et al. 2006; Leja et al. 2019a).

Due to the flexibility of the `continuity_sfh` model, the results are typically more reliable compared to the parametric fits. However, this extra parameter space is also more computationally expensive and most useful when it is constrained by high-quality data. Hence, we only apply this technique on nine host galaxies that are constraining enough to provide an accurate nonparametric SFH. The SED will encompass the observed photometry, observed photometry error, the model photometry, and model spectrum that depicts how well the model has been fit to the data.

4. Results

4.1. Host Properties in the Parametric Model

The results from the parametric fit are summarized in Table 2. The mass (M) and metallicity (Z) parameters are on log scales. For the analysis, we regroup galaxies into more general classes of Elliptical (E-) and Spiral (S-) type. The hosts in E-type group exhibit an average t_m of 5.95 Gyr and a median t_m of 5.42 Gyr, implying relatively older stellar populations with less star formation activities. Conversely, the average t_m is 3.85 Gyr and the median t_m is 3.48 Gyr for S-type galaxies. S-type galaxies exhibit an overall younger stellar population, though the range spans from 0.01–7.94 Gyr.

As mentioned in Section 3.1, the parametric SFR is described by a delayed exponentially declining function. Here, an SFR– M_* distribution is shown in Figure 4. The data points for the host of SN2007ke and SN2010et are different from others to distinguish upper limits on the SFR. For comparison, we also show the same metrics for Type Ia and stripped-envelope CC (SECC; Type IIb, Ib/c) SNe host galaxies from Childress et al. (2013) and Schulze et al. (2021), respectively. Similar to our analysis, the authors calculated the SFR and M_* using photometry, the Chabrier (2003) IMF, and an exponentially declining SFH in both works. We find that the distribution of Ca-rich host galaxies generally follows those of Type Ia and SECC SNe hosts, and tends to favor more massive hosts with lower SFRs. No clear preference between the host distributions of Type Ia and SECC SNe is observed. Notably, samples with higher stellar masses ($\log(M_*/M_\odot) > 10.5$) and lower metallicities ($\log(Z/Z_\odot) < \sim -0.10$) have low SFRs and are predominately E-type galaxies. Models from Yates et al. (2012) suggest that the galaxies may have undergone gradual dilution of gas phases after merger events, thereby halting further star formation.

Also displayed in Figure 4 is the host of PTF09dav as an outlier in the distribution. Such an offset from the distribution is in contrast with the fact that PTF09dav was classified to be a peculiar subluminal Type Ia SN (Sullivan et al. 2011). The galaxy has a disturbed morphology and nebular emission lines in the spectrum that are indicative of ongoing star formation (Sullivan et al. 2011), consistent with its high SFR and more aligned with SECC SNe host distribution than Type Ia.

In the case of iPTF16hgs in which the host is a low-metallicity, star-forming, spiral dwarf galaxy, De et al. (2018) found a stellar mass $\log(M_*/M_\odot) = 8.81 \pm 0.02$, a mean stellar population age of $0.2^{+0.63}_{-0.02}$ Gyr, and an integrated SFR of

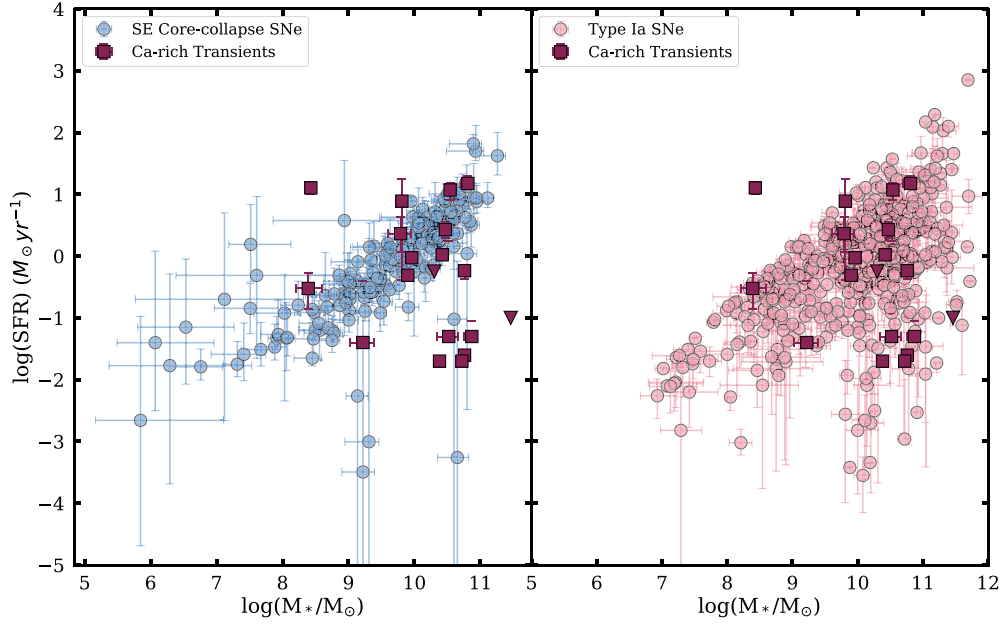


Figure 4. Distribution of SFR as a function of stellar mass of all host galaxies on log scales. 3σ upper limits of the SFR are displayed (\blacktriangledown) in the case of SN2007ke and SN2010et. Also shown are 167 SECC SNe host galaxies (blue; Schulze et al. 2021) and 442 Type Ia (pink; Childress et al. 2013) for comparison. Overall, the distribution of Ca-rich host galaxies displays no noticeable preference of galaxy populations for either type of SNe.

$0.5 M_{\odot} \text{ yr}^{-1}$. We compare our mass, metallicity, and stellar population age to that of De et al. (2018) and they are overall in good agreement with one another. The stellar mass from our parametric fit is slightly smaller at $\log(M_*/M_{\odot}) = 8.39$. However, parametric models are known to systematically underestimate stellar masses due to an offset from the true shape of the galaxy’s SFH (Carnall et al. 2019). The mean t_m from our analysis is 0.82 Gyr, just within the 1σ uncertainty from De et al. (2018). The significantly subsolar metallicity of $\approx 0.4 Z_{\odot}$ ($\log(Z/Z_{\odot}) = -0.38$) reported by De et al. (2018) also agrees with our result $\log(Z/Z_{\odot}) = -0.26$ within 1σ uncertainty. Although the SFR from De et al. (2018) is estimated from $H\alpha$ maps, we note that it is still consistent with our SFR derived from the parametric fit. The differences in our models and observational data compared to what was applied by De et al. (2018) can also explain the discrepancy between our results.

The metallicities of all Ca-rich transient host galaxies range between $\log(Z/Z_{\odot}) = -0.66$ and 18. In addition, we obtain an average stellar mass $\log(M_*/M_{\odot}) = 10.62$, with the a minimum mass of $\log(M_*/M_{\odot}) = 8.28$ and a maximum of $\log(M_*/M_{\odot}) = 11.46$. A subset (10) of our Ca-rich transient host galaxies were previously analyzed by Yuan et al. (2013). The authors converted observed K -band total luminosities of each host galaxy to stellar masses using numerical models of cosmic chemical evolution from Kobayashi et al. (2007) and found a range between $\log(M_*/M_{\odot}) = 10.08$ and 11.15 ($1.2 \times 10^{10} M_{\odot}$ – $1.4 \times 10^{11} M_{\odot}$). While most of our results fall within the range, the hosts of PTF09dav, SN2003dg, and SN2003dr are noticeably below the lower limit. Again, discrepancies in stellar mass likely arise from differences in methodologies and underlying assumptions.

In addition to the SFR, we also find the specific SFR (sSFR) defined as SFR per unit stellar mass for all host galaxies. We present the results in Figure 5. Galaxies at low redshifts are considered to be quiescent if their sSFR is $< 10^{-11} \text{ yr}^{-1}$

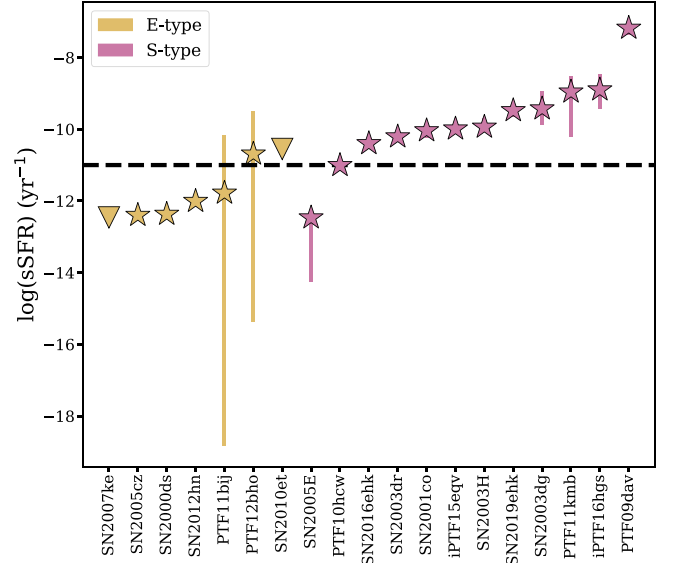


Figure 5. sSFR of all host galaxies with Ca-rich transients labeled on the x-axis. The red and dead threshold defined by Fontana et al. (2009) ($\text{sSFR} < -11 \text{ yr}^{-1}$) is shown as a black dashed line. E-type is marked in gold while S-type is marked in dark pink. The hosts of SN2005E and PTF10hcw are both disk galaxies that satisfy as red and dead. The $\log(\text{sSFR})$ for SN2007ke and SN2010et host galaxies are upper limits (\blacktriangledown).

(Fontana et al. 2009). Based on this quantitative threshold, we find that the majority of the E-type host galaxies have $\text{sSFR} < 10^{-11} \text{ yr}^{-1}$, labeling them as *red and dead*. The host of PTF12bho (gold) is an exception to this trend. Similarly, the hosts of 2005E and PTF10hcw, both disk galaxies, also do not obey the expected pattern as S-type galaxies. NGC 1032 (SN2005E) is an S0/a galaxy that is in the transition period between E and Sa galaxies on the stage sequence, while NGC 2639 (PTF10hcw) is an SAa galaxy. These two galaxies produce large bulge light and are considered early-type systems

Table 3
Host Galaxies' Stellar Population Properties for the Continuity Model

Transient	Host Galaxy	t_m Gyr	$\log(Z/Z_\odot)$	$\log(M_*/M_\odot)$	A_V mag	$\log(\text{SFR}_{\text{SED}})$ $M_\odot \text{ yr}^{-1}$
SN2000ds	NGC 2768	$8.77^{+0.42}_{-0.28}$	$-0.06^{+0.02}_{-0.02}$	10.92 ± 0.01	<0.004	$-1.82^{+0.10}_{-0.27}$
SN2001co	NGC 5559	$7.77^{+1.06}_{-0.77}$	$0.06^{+0.02}_{-0.04}$	10.66 ± 0.04	$0.90^{+0.15}_{-0.14}$	$0.34^{+0.16}_{-0.17}$
SN2003dr	NGC 5714	$9.96^{+1.26}_{-2.32}$	$0.06^{+0.03}_{-0.02}$	10.14 ± 0.05	$0.53^{+0.18}_{-0.02}$	$-0.12^{+0.07}_{-0.03}$
SN2005cz	NGC 4589	$9.22^{+0.56}_{-0.32}$	-0.23 ± 0.03	10.94 ± 0.01	$0.02^{+0.00}_{-0.01}$	$-2.05^{+0.19}_{-0.65}$
SN2012hn	NGC 2272	$8.26^{+0.37}_{-0.44}$	$-0.02^{+0.07}_{-0.08}$	10.58 ± 0.02	$0.01^{+0.02}_{-0.01}$	$-2.05^{+0.25}_{-0.48}$
SN2016hnk	MCG-01-06-070	$9.85^{+0.99}_{-1.93}$	0.09 ± 0.01	10.68 ± 0.02	$0.38^{+0.02}_{-0.04}$	$0.33^{+0.03}_{-0.04}$
SN2019ehk	NGC 4321	$4.83^{+1.63}_{-1.53}$	$0.06^{+0.03}_{-0.05}$	$10.81^{+0.07}_{-0.08}$	$0.56^{+0.07}_{-0.05}$	0.73 ± 0.18
PTF10hcv	NGC 2639	$7.47^{+0.82}_{-0.57}$	$-0.15^{+0.07}_{-0.10}$	11.05 ± 0.03	$0.40^{+0.13}_{-0.05}$	$-0.77^{+0.20}_{-0.41}$
iPTF15eqv	NGC 3430	$8.31^{+0.65}_{-0.77}$	$0.06^{+0.03}_{-0.05}$	$10.21^{+0.02}_{-0.03}$	$0.35^{+0.08}_{-0.05}$	$0.20^{+0.12}_{-0.07}$

Note. Median values and 1σ uncertainties of the posterior distributions using the `continuity_sfh` model. A 3σ upper limit on A_V is derived for NGC 2768. Similar to the parametric model, we fit for M_* , A_V , and Z . But unlike the function form imposed on the SFH by the parametric model, we use a time binning method in the nonparametric model, allowing greater flexibility to reproduce more accurate SFHs. We determine the SFR and t_m from the SFR ratios between adjacent time bins.

along the Hubble sequence with a strongly decreasing SFR, suggesting a dearth of new stars within the galaxies, resulting in a small sSFR (Sandage 1986). Zhou et al. (2021) also found that massive red spirals such as NGC 2639 and NGC 1032 and massive elliptical galaxies have very similar SFHs. This means that they have only experienced one major star formation episode early on (and possibly fast quenching). Overall, more than 50% of the host galaxies we examined exhibit some level of recent star formation that could support young star clusters.

4.2. Host Properties with a Nonparametric Model

We impose a nonparametric form of SFH to model the host galaxies of SN2000ds, SN2001co, SN2003dr, SN2005cz, SN2012hn, SN2016hnk, SN2019ehk, PTF10hcv, and iPTF15eqv. The sample contains three quiescent E-type galaxies (NGC 2768, NGC 4589, and NGC 2272) and six S-type galaxies (NGC 5559, NGC 5714, MCG-01-06-070, NGC 4321, NGC 2639, and NGC 3430). Each of these host galaxies has at least nine photometric values, which we found to be the minimum required for a confident analysis. We examine our results using the nonparametric model with various degrees of star formation activities and evaluate the effects on the stellar population properties. Parameters such as M_* and t_m are compared against metrics derived using the parametric model from Section 3.1.

The results of the nine host galaxy samples are shown in Table 3. The nine galaxies have an average t_m of 8.27 Gyr, pointing to old stellar populations in the host environment. We find all three of the E-type galaxies have subsolar metallicities with NGC 4589 being the most metal-poor. Conversely, almost all S-type galaxies have roughly the same super-solar metallicity. The nonparametric fits also show that the stellar masses of the four hosts are in the higher-mass range with the least massive being $\log(M_*/M_\odot) = 10.14$ (NGC 5714) and the most massive being $\log(M_*/M_\odot) = 11.05$ (NGC 2639) which are both S-type galaxies.

We find that S-type galaxies are much dustier, averaging $A_V = 0.52$ mag, unlike the quiescent galaxies in our sample. The dust extinction is an indicator of emission from young, massive stars and a higher SFR. Indeed, comparing $\log(\text{SFR})$ between E-type and S-type galaxies, we find a remarkably higher $\log(\text{SFR})$ in all S-type galaxies from the last 0–30 Myr as opposed to the three quiescent hosts. The recent and ongoing

star formation supports the possibility of a massive star progenitor behind the Ca-rich transient via core collapse. However, the quiescent galaxies in our sample with low SFRs in the recent years challenge applying this interpretation for all Ca-rich transients. Notably, Crocker et al. (2011) determined a SFR range for NGC 2768 between 0.025 and $0.195 M_\odot \text{ yr}^{-1}$, which is consistent with our findings.

To further evaluate our results from the nonparametric fits, we construct a panel of SFHs with SFR as a function of lookback time using eight temporal bins as shown in Figure 6. We find that the SFRs of E-type, quiescent galaxies, show steady exponential declines with very low present-day SFRs. These SFHs provide evidence that the majority of stellar mass has been formed during the earlier epoch and only a small fraction of the mass is contributed by the recent star formation activities. Since a large percentage of mass was formed in the earlier temporal bins, we find consistency in the t_m as most of the weight is determined by the older stellar population in the host galaxies. The SFH of four S-type galaxies also show a gradual decline in the galaxy's history. But unlike the E-type galaxies, the SFRs became roughly constant and displayed a slight increase <1 Gyr ago in lookback time. The climb in SFRs represents an association with new births of massive young stars within the host environment. NGC 2639 is a type SAa, Seyfert galaxy with LINER nuclear activity (Lunnan et al. 2017; Sebastian et al. 2019). Its SFH is more similar to E-type galaxies with an apparent exponential decline and decreasing SFRs. This agrees with the result that NGC 2639 has the lowest recent SFR out of all S-type galaxy samples. Sebastian et al. (2019) estimated a SFR on the order of $1 M_\odot \text{ yr}^{-1}$ from Spitzer infrared fluxes, which is consistent with the low SFR found in the nonparametric fit. The morphology of the galaxy could indicate a past gas-rich merger that caused the drop in SFR (Sebastian et al. 2019).

Stellar population analysis was performed by Galbany et al. (2019) on the host galaxy of SN2016hnk using integral field spectroscopy. The authors report a stellar mass $\log(M_*/M_\odot) = 10.68$, which is equivalent to our result ($\log(M_*/M_\odot) = 10.68$). We applied a -0.24 dex correction (Mitchell et al. 2013) to the stellar mass since a Chabrier IMF is used in this work as opposed to a Salpeter IMF (Salpeter 1955). The corrected stellar mass for the host of SN2016hnk is still comparable to our results. Galbany et al. (2019) also derived an average stellar age = 690 Myr, $\text{SFR} = 0.65 M_\odot \text{ yr}^{-1}$, and $A_V = 0.02$ mag for

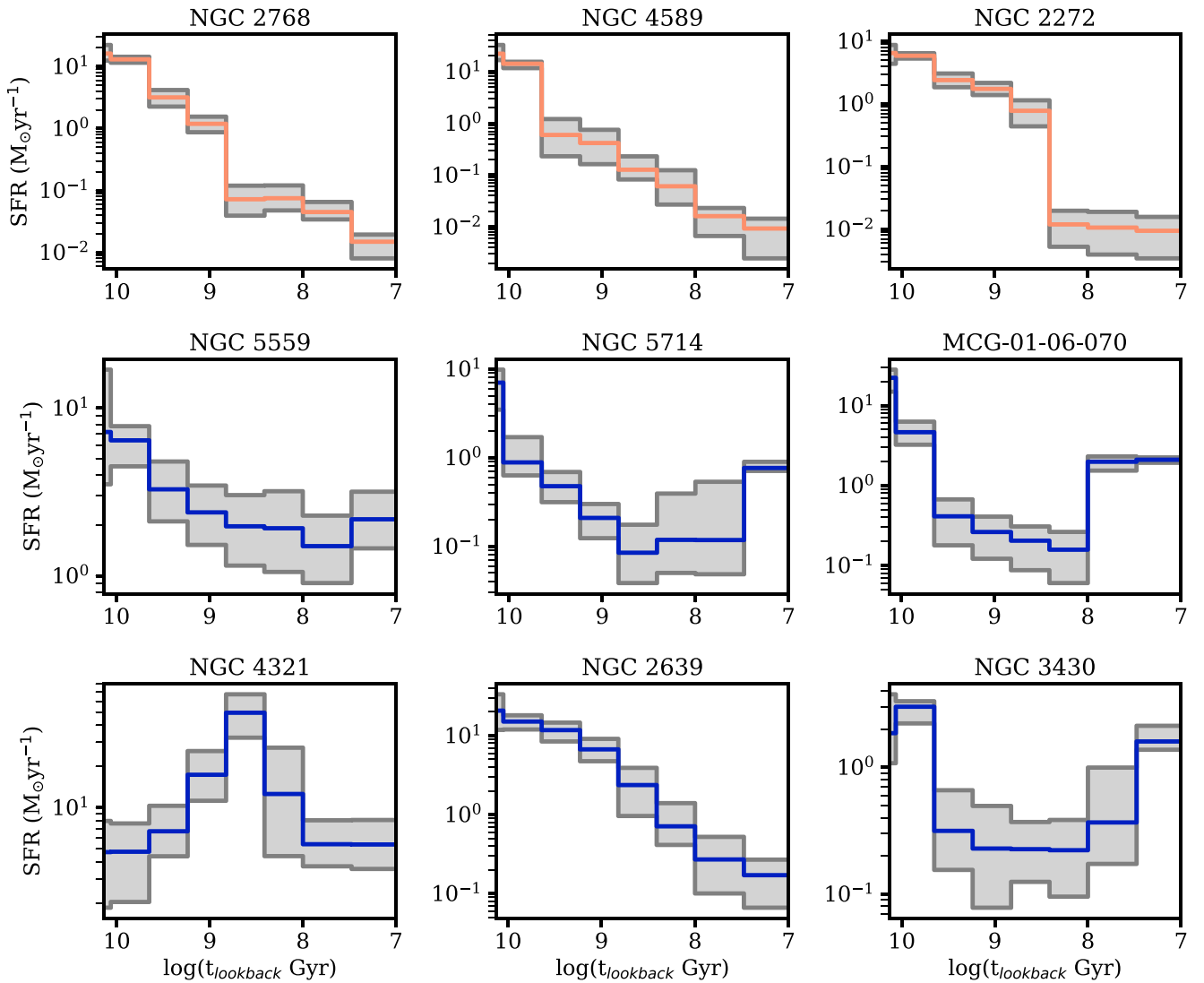


Figure 6. The SFH of nine host galaxies constructed using the nonparametric `continuity_sfh` model. The quiescent galaxies (NGC 2768, NGC 4589, and NGC 2272) have constant declines in the SFR with no recent burst of star formation. This contrasts with the star-forming galaxies, which shows evidence for a recent increase in SFR. One exception is NGC 2639 which resembles the steady decrease in SFRs found for E-type galaxies, and is consistent with our finding that it has the lowest SFR compared to other S-type galaxies in our sample.

MCG-01-06-070. The reported age is light-weighted and cannot be directly compared with the mass-weighted age in our analysis, as light-weighted ages are always younger than mass-weighted determinations. Using the nonparametric `continuity_sfh` model, we find SN2016hkn’s host galaxy to be dustier and more star forming in comparison. Broadly, the discrepancies are likely due to differing models of SFH and underlying assumptions. Although Galbany et al. 2019 employed a nonparametric SFH, they utilized STARLIGHT (Cid Fernandes et al. 2005; López Fernández et al. 2016) on the integrated spectrum of host galaxy to estimate the fractional contribution of different SSP instead of fitting photometric data to a nonparametric model.

5. Discussion

5.1. Comparing Parametric and Nonparametric Results

The parametric and nonparametric `continuity_sfh` model are two distinctly different templates with varying stellar population metrics. The most notable difference is the

fact that parametric SFH assumes a delayed τ function form for $SFR(t)$ whereas the nonparametric model does not. The use of two different models allows us to examine the influence of our choice of priors and observational data on the inferred properties. So, it is pertinent that we compare the results from each model to extract more information from the SED fitting.

We first consider the effects on the mass-weighted age. Carnall et al. (2019) demonstrated that the parametric model underestimates stellar population age and favors galaxy formation at later times. Comparing t_m of all nine host galaxies in each model, we find that the mass-weighted stellar ages obtained from the `continuity_sfh` model are consistently older than what was derived using the parametric model, in agreement with the finding that parametric models systematically underestimate galaxy ages (Wuyts et al. 2011). The stellar population was found to be older in the nonparametric model by at least 1.5 Gyr with the largest offset being 4.44 Gyr, more than double the mass-weighted age from the parametric results. The fact that the parametric model struggles to obtain a better estimate for t_m is due to its strong dependency on priors

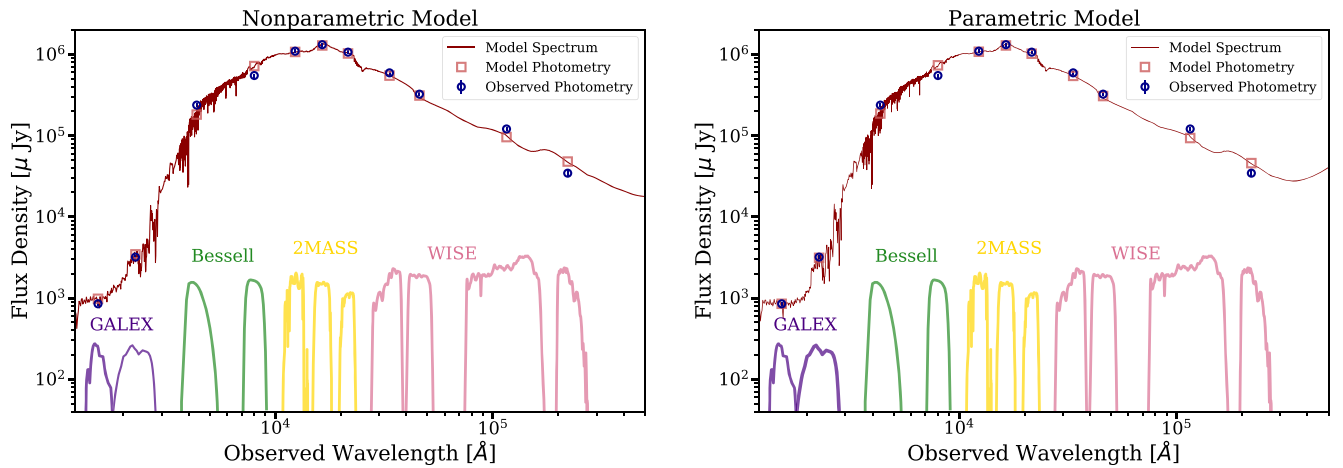


Figure 7. The broadband photometry of the host of SN2000ds ranging from optical to FIR (blue data points), and best-fit model spectrum and model photometry (red line and square data points) from the nonparametric (left) and parametric model fitting (right). There is an excellent consistency in the observed optical photometry, model photometry, and features. GALEX *UV*-band, Bessell *BI*-band, 2MASS *JHK*-band, and WISE *W1W2W3W4*-band filter response curves are used in both fits.

and the priors tendency to prefer recent star formation despite a more predominant contribution from the older stars in the overall stellar masses (Lower et al. 2020). Additionally, the `continuity_sfh` model produces better stellar population ages when fit to simulations, outperforming the parametric model by producing a more realistic age for the host environments (Lower et al. 2020).

Stellar mass is generally considered the most robust metric derived from SED fitting. Nonparametric SFHs are found to recover stellar masses with higher accuracy attributable to its flexibility (Lower et al. 2020). The parametric model, on the other hand, underestimates stellar masses due to difficulty in fine-tuning the prior for the SFR. Analysis from Carnall et al. (2019) reported a ~ 0.3 dex uncertainties for stellar mass property while Lower et al. (2020) found an average offset in stellar mass from the parametric model to be 0.38 dex with an average uncertainty of 0.19 dex when compared to simulated galaxies. Our results show that both the E-type and S-type galaxies from our sample have a lower M_* with comparable uncertainty range in the parametric model compared to the `continuity_sfh` model, consistent with the fact that parametric models tend to underestimate stellar masses (Carnall et al. 2019; Lower et al. 2020). This also agrees with the finding that nonparametric SFH models infer an older stellar population age, which, in turn, produces a higher stellar mass (Leja et al. 2019b). Additionally, the stellar mass between the two models from our sample differ by an average of 0.23 dex and this bias comes from differences in the assumed SFH models.

We now consider the SFRs inferred in our sample. It is important to differentiate that the SFR found in the parametric model is derived from the overall stellar population age, while the nonparametric SFRs reported are only within the youngest age bin, i.e., 0–30 Myr in lookback time. We find that the parametric model routinely offset from the nonparametric SFH model, ranging between 0.1 and 0.55 dex. This places the bias within the systematic uncertainties of ~ 0.5 dex typically assumed for SFR measurements (Pacifi et al. 2015). The parametric model predicted higher SFRs for six out of nine hosts including all three quiescent galaxies. This is related to the model’s strong bias by the SFH priors compared to other metrics such as stellar mass and dependence on the SFH over more recent years in the galaxy histories (Carnall et al. 2019).

Nonetheless, both models infer a low $SFR(t)$ for the quiescent, E-type galaxies and moderate $SFR(t)$ for the star-forming, S-type galaxy.

The evolution of SFRs with respect to the lookback times as shown in Figure 6 demonstrates that an exponentially declining function such as the delayed- τ model is, in fact, suitable for quiescent galaxies with very old ages. However, the short-coming of applying the delayed- τ SFH model to galaxies is the false constraints imposed on galaxy properties by the SFH priors. In this case, the nonparametric model is a more promising alternative that provides greater flexibility than parametric models, and allows more direct incorporation of prior beliefs (Lower et al. 2020). As a consequence, it produces a more accurate SFH, especially with more bursty SFHs.

To illustrate the quality of our model fits, we display the SED of NGC 2768 using each model in Figure 7. The SED coverage spans from UV (GALEX) to far-IR (FIR; WISE), representing the full broadband data set which impacts the accuracy of the galaxy properties inferred from SED fitting. The shape of the SED resembles the SEDs for mock galaxies with a falling SFH in Figure 2 of the analysis by Carnall et al. (2019). The SED shape is used to constrain parameters such as metallicity, sSFR, and dust attenuation (Conroy 2013). The differences in stellar mass and metallicity from our analysis suggest that the SED from the parametric model offsets from the one in the `continuity_sfh` model. However, they both agree with the exponentially declining SFH shown in Figure 6.

In addition, the mass-weighted age is also dependent on the shape of the SED. We compare the average stellar population age with published results that range widely from 4–11 Gyr (Amblard et al. 2017). Our results most closely resemble the age of 8.0 ± 3.5 Gyr calculated by Denicoló et al. (2005). Age is often known to be degenerate with dust unless spectroscopy or FIR data is available that can robustly measure the dust attenuation (Conroy 2013). We obtained a 3σ upper limit on A_V in both models. The results illustrate that NGC 2768 is indeed, an old and non-dusty environment with a strong constraint of $A_V < 0.004$ mag derived from the nonparametric model.

As mentioned in Section 3, we included dust emission in both models for NGC 2768 in order to better fit IR photometry. The observed broadband photometry from both SEDs are consistent with the model photometry. We also observe

Table 4
Host galaxy SN Rates and Probabilities of Core-collapse versus Type Ia Origin

Transient	Host Galaxy	CC SN/yr	Ia SN/yr	P_{cc}	P_{Ia}
SN2000ds	NGC 2768	$(3.6^{+1.0}_{-0.7}) \times 10^{-4}$	$(7.9^{+0.9}_{-0.8}) \times 10^{-3}$	$0.04^{+0.01}_{-0.01}$	$0.96^{+0.01}_{-0.01}$
SN2001co	NGC 5559	$(2.7^{+0.8}_{-0.6}) \times 10^{-2}$	$(7.8^{+1.7}_{-1.4}) \times 10^{-3}$	$0.77^{+0.05}_{-0.06}$	$0.23^{+0.06}_{-0.05}$
SN2003dr	NGC 5714	$(7.0^{+0.7}_{-0.5}) \times 10^{-3}$	$(1.3^{+0.5}_{-0.3}) \times 10^{-3}$	$0.85^{+0.03}_{-0.05}$	$0.15^{+0.05}_{-0.03}$
SN2005cz	NGC 4589	$(2.4^{+2.3}_{-1.1}) \times 10^{-4}$	$(7.5^{+1.3}_{-1.1}) \times 10^{-3}$	$0.03^{+0.03}_{-0.01}$	$0.97^{+0.01}_{-0.03}$
SN2012hn	NGC 2272	$(1.7^{+1.5}_{-0.7}) \times 10^{-4}$	$(4.6^{+0.5}_{-0.4}) \times 10^{-3}$	$0.03^{+0.03}_{-0.02}$	$0.97^{+0.02}_{-0.03}$
SN2016hnk	MCG-01-06-070	$(2.6^{+0.3}_{-0.2}) \times 10^{-2}$	$(4.6^{+1.1}_{-0.8}) \times 10^{-3}$	$0.85^{+0.02}_{-0.03}$	$0.15^{+0.03}_{-0.02}$
SN2019ehk	NGC 4321	$(7.8^{+2.3}_{-1.7}) \times 10^{-2}$	$(4.1^{+1.4}_{-1.0}) \times 10^{-2}$	$0.65^{+0.07}_{-0.07}$	$0.35^{+0.07}_{-0.07}$
PTF10hwc	NGC 2639	$(3.6^{+2.8}_{-1.3}) \times 10^{-3}$	$(1.6^{+0.3}_{-0.2}) \times 10^{-2}$	$0.18^{+0.1}_{-0.07}$	$0.82^{+0.07}_{-0.1}$
iPTF15eqv	NGC 3430	$(1.5^{+0.2}_{-0.2}) \times 10^{-2}$	$(2.0^{+0.5}_{-0.4}) \times 10^{-3}$	$0.89^{+0.02}_{-0.03}$	$0.11^{+0.03}_{-0.02}$

absorption lines from the model spectra which is typical for a quiescent galaxy with sparse star formation.

5.2. SN Rates

We can quantitatively predict SN rates in our galaxies from the aforementioned SFHs using known forms of the SN delay-time distribution (DTD), defined as the SN rate per unit mass of formed stars as a function of time elapsed since a hypothetical *burst* of star formation (Maoz & Mannucci 2012). Theoretically, the DTD depends sensitively on the stellar evolution channels of the progenitor stars (Mennekens et al. 2010; Toonen et al. 2012; Eldridge et al. 2017; Zapartas et al. 2017), and has been extensively used to validate the progenitor channels of Type Ia SNe (Totani et al. 2008; Maoz & Badenes 2010; Maoz & Sharon 2010; Maoz et al. 2011, 2012; Graur et al. 2014; Maoz et al. 2014; Maoz & Graur 2017). While measuring a Ca-rich transient DTD is not feasible with our small, heterogenous sample, we can use existing constraints on the Type Ia and core-collapse SN DTD, convolve them with our measured SFHs, and roughly estimate the probability that the Ca-rich transients are from a Type Ia-like or core-collapse-like progenitor origin.

We restrict this analysis to the nine galaxies with nonparametric SFHs in Table 3, since the parametric SFHs may significantly underestimate the recent SFH and CC SN rates for star-forming galaxies. For each galaxy’s SFH ($\dot{M}(t)$ in units of M_{\odot}/yr), the SN rate in a galaxy observed at a cosmic time (t) can be evaluated using

$$R_{\text{sn}}(t) = \int_0^t \dot{M}(t - t_d) \Psi(t_d) dt_d,$$

where $\Psi(t_d)$ is the DTD for either CC or Type Ia SN as a function of delay time t_d (Maoz & Badenes 2010), and $R_{\text{sn}}(t)$ is the SN rate at a given cosmic time t . For each age bin j and corresponding SFR from the nonparametric model, the integral can be spread as

$$R_{\text{sn}} = \sum_{j=1}^{N_{\text{age}}} \dot{M}_j \int_{t_{jl}}^{t_{ju}} \Psi(t_d) dt_d,$$

where N_{age} is the number of age bins in the SFH, and t_{ju} , t_{jl} are the upper and lower bounds of each age bin. Since \dot{M} is constant in each age bin, it appears outside the integral.

For core-collapse SNe, we use the form of $\Psi(t_d)$ in Equation A2 of Zapartas et al. (2017). The DTD is similar to the case of single stellar evolution for $t_d < 40$ Myr, with the exception of a *delayed* core-collapse SN channel at $t_d = 40$ – 200 Myr produced by stellar mergers of 4 – $8 M_{\odot}$ stars (this channel

however only accounts for 7%–22% of CC SN population). For Type Ia SNe, we assume the form of $\Psi(t_d)$ constrained by Maoz & Mannucci (2012) from SN Ia surveys, i.e., $\Psi(t_d) = 4 \times 10^{-13} \text{ SN yr}^{-1} M_{\odot}^{-1} (t_d/1 \text{ Gyr})^{-1}$ for $t_d > 40$ Myr. With the measured SN rates of core-collapse (R_{cc}) and Type Ia (R_{Ia}), we quantify the probability that the Ca-rich transient in each galaxy is a SN Ia or core-collapse event as $p_{\text{cc}} = R_{\text{cc}}/(R_{\text{cc}} + R_{\text{Ia}})$ and $p_{\text{Ia}} = 1 - p_{\text{cc}}$. These quantities will have uncertainties due to the uncertainties in the measured SFHs. We propagate these uncertainties using a Monte Carlo method. For each galaxy, we generate 5×10^4 randomized SFHs assuming a log-normal distribution of SFRs for each age bin. We then calculate the SN rates and probabilities for each of these randomized SFHs, and measure the median, 16th and 84th percentiles of the distributions.

The CC and SNe Ia rates and their probabilities for each of the nine host galaxies are summarized in Table 4. The SNe Ia rate from quiescent galaxies (NGC 2768, NGC 4589, and NGC 2272) are nearly 20–30 times higher than the CC SN rates, with less than a 5% probability respectively that the Ca-rich transients originate from massive progenitor systems. The star-forming galaxies in our nonparametric SFH sample, as expected, show a higher probability of producing CC SNe, excluding the host of PTF10hwc, which has a relatively lower SFR.

Because only nine Ca-rich transient host galaxies could be modeled with a nonparametric SFH, our ability to draw conclusions about the entire population of Ca-rich transients is limited. Nonetheless, our analysis uncovered three examples where a core-collapse origin is improbable (<5%). Thus, our work supports the notion that the progenitor population of Ca-rich transients do not come exclusively from core-collapse explosions, and must either be only from WD stars or a mixed population of WD stars with other channels, potentially including massive star explosions. The fraction of CC versus Type Ia origin can be quantified more accurately in subsequent studies with larger, homogeneous Ca-rich transient sample and with spatially-resolved star formation histories of the galaxies, giving a more accurate age distribution of the SN progenitor (Maoz & Badenes 2010; Chen et al. 2021; Sarbadhicary et al. 2021). Improvements can also be made by utilizing better DTDs of potential progenitor channels. Instead of using the DTDs of SNe Ia and CC as proxies of Ca-rich transients as we have here, it would be advantageous to employ DTDs that are derived directly from theoretical models of proposed Ca-rich progenitor channels.

6. Conclusions

In this paper we have presented multiwavelength observations of the host galaxies for all known Ca-rich transients and

an uniform treatment of the stellar population modeling using PROSPECTOR. The use of two separate models (parametric versus nonparametric) allows us to compare and evaluate the effect of assumptions made in the stellar population properties. We reach the following conclusions:

1. From our SED fitting of all host galaxies using the parametric model, the average mass-weighted age for E-type host galaxies is 5.95 Gyr and 3.85 Gyr for S-type galaxies.
2. $\approx 42\%$ of all hosts, including two S-type host galaxies, can be considered as red and dead (e.g., $sSFR < 10^{-11} \text{ yr}^{-1}$; Fontana et al. 2009), deeming them quiescent. This suggests that star formation has been suppressed in these host environments and that they are not associated with young massive stars.
3. We performed nonparametric SED fitting using the `continuity_sfh` model for the host galaxies of SN2000ds, SN2001co, SN2003dr, SN2005cz, SN2012hn, SN2016hnk, SN2019ehk, PTF10hcz, and iPTF15eqv (three E-type and six S-type). We find that the mass-weighted ages and the stellar populations of the host galaxies are consistently older and more massive, respectively, compared to results from the parametric model. Further, the majority of stellar population mass was formed in the first few gigayears of the hosts' lifetimes and therefore the t_m weighs them more heavily than stars that are born in later years.
4. We construct the SFH of our nonparametric fits and find that the E-type galaxies exhibit exponentially declining SFH as expected for older stellar populations, with no evidence of recent (< 100 Myr) bursts of star formation. The S-type galaxies show recent star formation in the last 30 Myr (except NGC 2639) with an overall significantly higher SFR compared to the E-type hosts.
5. Among the nine galaxies we are able to perform a detailed (nonparametric) SFH, we estimate a $< 5\%$ probability for three separate host galaxies that the Ca-rich transients originated from a core-collapse explosion, taking into account known forms of the Type Ia and core-collapse SN DTDs. Thus, we find it very unlikely that the progenitor population of Ca-rich transients originates exclusively from core-collapse explosions.

Our work supports the notion that the progenitors of Ca-rich transients must either be only from WD stars or a mixed population of WD stars with other channels, potentially including massive star explosions. Moving forward, the addition of spectra and/or narrowband photometry to our fits can improve the mass recovery of stellar populations and better constrain age, metallicity, and early star formation activities (Conroy 2013; Lower et al. 2020). The availability of more broadband photometry will also be advantageous for nonparametric techniques that offer SFH reconstruction methods with

unbiased priors. Especially desirable is explosion site spectroscopy of larger samples of Ca-rich host galaxies, since parameters inferred for the hosts may not accurately reflect those of the Ca-rich transient environments, given that some are far offset from the optical radius. DTD models of proposed Ca-rich transient progenitors are also needed to quantitatively predict rates more accurately.

Our method of photometry-only population inferencing will remain a primary way of investigating numerous Ca-rich transient host galaxies at high redshift. This is important because there is the concern that the present distribution of early-type and late-type host galaxies of Ca-rich is influenced by selection effects (Lunnan et al. 2017), and larger numbers of Ca-rich transients discovered in un-targeted surveys are needed. The Vera Rubin Observatory, which will discover thousands Ca-rich transients over the course of its 10 yr all-sky transient survey, has the potential to mitigate these selection biases and provide quality photometric data from which to perform nonparametric fits and best constrain the presently debated ratio of dwarf versus massive star progenitor populations.

D.M. acknowledges NSF support from grants PHY-1914448 and AST-2037297. We are grateful to Samir Salim for useful discussions of photometric data and catalog usage. Y.D. thanks Niharika Sravan, Mark Linvill, Alexander M. Warner, and Nabeel Rehemtulla for programming and plotting assistance. W.J-G is supported by the National Science Foundation Graduate Research Fellowship Program under grant No. DGE-1842165. W.J-G acknowledges support through NASA grants in support of Hubble Space Telescope programs GO-16075 and GO-16500. S.K.S. acknowledges support from NSF AST-1907790 and the Packard Foundation. This research has made use of data products from the Two Micron All Sky Survey, which is a joint project of the University of Massachusetts and the Infrared Processing and Analysis Center/California Institute of Technology, funded by the National Aeronautics and Space Administration and the National Science Foundation. We also used the NASA/IPAC Extragalactic Database, which is funded by the National Aeronautics and Space Administration and operated by the California Institute of Technology.

This research is based on observations made with the NASA/ESA Hubble Space Telescope obtained from the Space Telescope Science Institute, which is operated by the Association of Universities for Research in Astronomy, Inc., under NASA contract NAS 526555.

Software: `Prospector` (Leja et al. 2017), `Python-fsps` (Conroy & Gunn 2010; Foreman-Mackey et al. 2014), `dynesty` (Speagle 2020), `SAOImage DS9` (Joye & Mandel 2003).

Appendix

Table 5 lists all photometry used in our analysis of the host galaxies of Ca-rich transients.

Table 5
Ca-rich Transients Host Galaxy Photometry

Host	Transient	R.A. (J2000)	Decl. (J2000)	Filter	$m_{AB}^{a,b}$	References. ^c				
NGC 2768	SN2000ds	09 ^h 11 ^m 37.50 ^s	+60°02′14″0	FUV	16.578 ± 0.003	1				
				NUV	15.140 ± 0.001	1				
				B	10.460 ± 0.020	2				
				I	9.550 ± 0.030	2				
				J	8.800 ± 0.020	2				
				H	8.600 ± 0.030	2				
				K	8.830 ± 0.030	2				
				W1	9.647 ± 0.0001	1				
				W2	10.124 ± 0.0003	1				
				W3	11.1950 ± 0.009	1				
				W4	12.556 ± 0.111	1				
				NGC 5559	SN2001co	14 ^h 19 ^m 12.79 ^s	+24°47′55″42	FUV	17.551 ± 0.001	1
								NUV	16.960 ± 0.001	1
								g	14.326 ± 0.005	3
r	13.516 ± 0.005	3								
i	13.059 ± 0.005	3								
z	12.781 ± 0.005	3								
J	12.348 ± 0.020	4								
H	12.209 ± 0.020	4								
K	12.209 ± 0.031	4								
W1	12.758 ± 0.0003	1								
W2	13.259 ± 0.001	1								
W3	11.741 ± 0.003	1								
W4	11.434 ± 0.008	1								
NGC 2207	SN2003H	06 ^h 16 ^m 22.03 ^s	−21°22′21″60					FUV	12.803 ± 0.001	1
				NUV	12.439 ± 0.0001	1				
				B	11.700 ± 0.300	2				
				I	10.090 ± 0.100	2				
				W1	10.045 ± 0.0001	1				
				W2	10.545 ± 0.0003	1				
				W3	8.629 ± 0.001	1				
				W4	7.964 ± 0.001	1				
				UGC 6934	SN2003dg	11 ^h 57 ^m 31.83 ^s	−01°15′10″58	FUV	18.00 ± 0.01	2
								NUV	17.59 ± 0.01	2
								J	13.49 ± 0.04	2
								H	13.23 ± 0.05	2
								K	13.44 ± 0.08	2
								NGC 5714	SN2003dr	14 ^h 38 ^m 11.52 ^s
NUV	15.952 ± 0.002	1								
g	13.924 ± 0.005	3								
r	13.149 ± 0.005	3								
i	12.749 ± 0.005	3								
z	12.448 ± 0.005	3								
J	12.032 ± 0.022	3								
H	11.722 ± 0.031	3								
K	11.902 ± 0.035	3								
W1	12.294 ± 0.0004	1								
W2	12.810 ± 0.001	1								
W3	11.364 ± 0.004	1								
W4	11.082 ± 0.012	1								
NGC 1032	SN2005E	02 ^h 39 ^m 23.64 ^s	+01°05′37″64	NUV	16.229 ± 0.018	1				
				g	11.786 ± 0.005	5				
				r	10.955 ± 0.005	5				
				z	10.234 ± 0.005	5				
				W1	10.869 ± 0.0002	1				
				W2	11.495 ± 0.001	1				
				W3	11.686 ± 0.008	1				
				W4	11.661 ± 0.026	1				

Table 5
(Continued)

Host	Transient	R.A. (J2000)	Decl. (J2000)	Filter	$m_{AB}^{a,b}$	References. ^c
NGC 4589	SN2005cz	$12^h37^m24.99^s$	$+74^\circ11'30''.92$	FUV	17.614 ± 0.003	1
				NUV	15.904 ± 0.001	1
				J	9.742 ± 0.016	4
				H	9.516 ± 0.016	4
				K	9.755 ± 0.017	4
				W1	10.312 ± 0.0001	1
				W2	10.997 ± 0.0002	1
				W3	12.207 ± 0.009	1
				W4	12.453 ± 0.039	1
NGC 1129	SN2007ke	$02^h54^m27.38^s$	$+41^\circ34'46''.52$	NUV	18.400 ± 0.150	6
				u	14.526 ± 0.005	3
				g	12.471 ± 0.005	3
				r	11.589 ± 0.005	3
				i	11.144 ± 0.005	3
				z	10.873 ± 0.005	3
CGCG 170-011	SN2010et	$17^h16^m52.18^s$	$+31^\circ35'02''.88$	g	14.784 ± 0.005	3
				r	14.040 ± 0.005	3
				i	13.619 ± 0.005	3
				z	13.355 ± 0.005	3
				J	13.499 ± 0.041	4
				H	13.290 ± 0.026	4
				K	13.558 ± 0.017	4
NGC 2272	SN2012hn	$06^h42^m41.30^s$	$-27^\circ27'34''.20$	FUV	17.667 ± 0.021	1
				NUV	16.227 ± 0.005	1
				J	10.581 ± 0.023	4
				H	10.402 ± 0.027	4
				K	10.648 ± 0.034	4
				W1	11.178 ± 0.0002	1
				W2	11.861 ± 0.001	1
				W3	12.609 ± 0.014	1
				W4	14.231 ± 0.227	1
MGC-01-06-070	SN2016hnk	$02^h13^m15.79^s$	$-07^\circ39'42''.70$	FUV	16.182 ± 0.001	1
				NUV	15.825 ± 0.001	1
				g	14.339 ± 0.005	3
				r	13.517 ± 0.005	3
				i	13.095 ± 0.005	3
				z	12.781 ± 0.005	3
				W1	12.723 ± 0.001	1
				W2	13.401 ± 0.002	1
				W3	12.926 ± 0.014	1
NGC 4321	SN2019ehk	$12^h22^m54.831^s$	$+15^\circ49'18''.54$	FUV	12.547 ± 0.0001	1
				NUV	11.998 ± 0.00004	1
				J	8.593 ± 0.016	4
				H	8.463 ± 0.018	4
				K	8.650 ± 0.018	4
				W1	8.950 ± 0.0001	1
				W2	9.471 ± 0.0002	1
				W3	7.808 ± 0.001	1
				W4	7.412 ± 0.002	1
2MASX J22465295 + 2138221	PTF09dav	$22^h46^m52.95^s$	$+21^\circ38'21''.90$	g	17.931 ± 0.064	7
				r	17.588 ± 0.087	7
				i	17.227 ± 0.064	7
				y	16.621 ± 0.123	7
				J	15.329 ± 0.083	4
				H	15.109 ± 0.075	4
				K	15.374 ± 0.149	4
NGC 2639	PTF10hcw	$08^h43^m38.08^s$	$+50^\circ12'20''.00$	FUV	16.961 ± 0.001	1
				NUV	15.908 ± 0.001	1
				g	12.100 ± 0.005	3
				r	11.225 ± 0.005	3
				i	10.871 ± 0.005	3
				z	10.515 ± 0.005	3
				J	10.392 ± 0.016	4
				H	10.159 ± 0.016	4
				K	10.159 ± 0.016	4
				W1	10.340 ± 0.016	4
				W2	10.963 ± 0.0001	1
				W3	11.589 ± 0.0004	1
				W4	11.101 ± 0.003	1
	10.796 ± 0.008	1				

Table 5
(Continued)

Host	Transient	R.A. (J2000)	Decl. (J2000)	Filter	$m_{AB}^{a,b}$	References. ^c
IC 3956	PTF11bij	$12^{\text{h}}58^{\text{m}}56.38^{\text{s}}$	$+37^{\circ}23'53''.44$	J	13.926 ± 0.030	4
				H	13.707 ± 0.037	4
				K	13.858 ± 0.050	4
				W1	14.337 ± 0.005	5
				W2	14.987 ± 0.005	5
NGC 7265	PTF11kmb	$22^{\text{h}}22^{\text{m}}27.44^{\text{s}}$	$+36^{\circ}12'34''.58$	NUV	18.500 ± 0.066	6
				g	14.471 ± 0.016	7
				r	14.351 ± 0.038	7
				i	13.527 ± 0.050	7
WISEA J130109.43 + 280159.1	PTF12bho	$13^{\text{h}}01^{\text{m}}09.44^{\text{s}}$	$+28^{\circ}01'59''.21$	g	17.409 ± 0.007	7
				r	16.711 ± 0.027	7
				i	16.399 ± 0.059	7
				z	16.189 ± 0.027	7
				y	15.937 ± 0.022	7
NGC 3430	iPTF15eqv	$10^{\text{h}}52^{\text{m}}11.40^{\text{s}}$	$+32^{\circ}57'01.56$	FUV	14.089 ± 0.0002	1
				NUV	13.769 ± 0.0002	1
				g	12.570 ± 0.005	3
				r	11.795 ± 0.005	3
				i	11.391 ± 0.005	3
				z	11.185 ± 0.005	3
				J	10.836 ± 0.014	4
				H	10.651 ± 0.018	4
				K	10.869 ± 0.024	4
				W1	11.285 ± 0.0003	1
				W2	11.867 ± 0.001	1
				W3	10.119 ± 0.003	1
				W4	9.817 ± 0.007	1
				2MASX J00505254 + 2722432	iPTF16hgs	$00^{\text{h}}50^{\text{m}}52.55^{\text{s}}$
r	17.015 ± 0.036	7				
J	16.227 ± 0.059	4				
H	16.119 ± 0.037	4				
K	16.148 ± 0.024	4				

Notes.^a Corrected for Galactic extinction (Schlegel et al. 1998) except W3 and W4.^b An uncertainty of 0.005 was imposed on SDSS and DESI photometry.^c (1) Leroy et al. (2019), (2) Bai et al. (2015), (3) SDSS, (4) 2MASS, (5) DESI, (6) GALEX, (7) Pan-STARRS DR2.**ORCID iDs**Yuxin Dong (董雨欣)  <https://orcid.org/0000-0002-9363-8606>Dan Milisavljevic  <https://orcid.org/0000-0002-0763-3885>Joel Leja  <https://orcid.org/0000-0001-6755-1315>Sumit K. Sarbadhickey  <https://orcid.org/0000-0002-4781-7291>Anya E. Nugent  <https://orcid.org/0000-0002-2028-9329>Raffaella Margutti  <https://orcid.org/0000-0003-4768-7586>Wynn V. Jacobson-Galán  <https://orcid.org/0000-0003-1103-3409>Abigail Polin  <https://orcid.org/0000-0002-1633-6495>John Banovetz  <https://orcid.org/0000-0003-0776-8859>Bhagya Subrayan  <https://orcid.org/0000-0001-8073-8731>**References**

Albaret, F. D., Allende Prieto, C., Almeida, A., et al. 2017, *ApJS*, 233, 25
 Alsing, J., Peiris, H., Leja, J., et al. 2020, *ApJS*, 249, 5
 Amblard, A., Temi, P., Gaspari, M., & Brighenti, F. 2017, *ApJ*, 834, 20
 Bai, Y., Zou, H., Liu, J., & Wang, S. 2015, *ApJS*, 220, 6
 Bildsten, L., Shen, K. J., Weinberg, N. N., & Nelemans, G. 2007, *ApJL*, 662, L95
 Bobrick, A., Davies, M. B., & Church, R. P. 2017, *MNRAS*, 467, 3556
 Boquien, M., Burgarella, D., Roehlly, Y., et al. 2019, *A&A*, 622, A103
 Calzetti, D., Armus, L., Bohlin, R. C., et al. 2000, *ApJ*, 533, 682

Cardelli, J. A., Clayton, G. C., & Mathis, J. S. 1989, *ApJ*, 345, 245
 Carnall, A. C., Leja, J., Johnson, B. D., et al. 2019, *ApJ*, 873, 44
 Chabrier, G. 2003, *PASP*, 115, 763
 Chen, X., Hu, L., & Wang, L. 2021, *ApJ*, 922, 15
 Childress, M., Aldering, G., Antilogus, P., et al. 2013, *ApJ*, 770, 107
 Cid Fernandes, R., Mateus, A., Sodré, L., Stasińska, G., & Gomes, J. M. 2005, *MNRAS*, 358, 363
 Clausen, D., & Eracleous, M. 2011, *ApJ*, 726, 34
 Conroy, C. 2013, *ARA&A*, 51, 393
 Conroy, C., & Gunn, J. E. 2010, Flexible Stellar Population Synthesis, Astrophysics Source Code Library, ascl:1010.043
 Conroy, C., Gunn, J. E., & White, M. 2009, *ApJ*, 699, 486
 Crocker, A. F., Bureau, M., Young, L. M., & Combes, F. 2011, *MNRAS*, 410, 1197
 da Cunha, E., Charlot, S., & Elbaz, D. 2008, *MNRAS*, 388, 1595
 De, K., Fremling, U. C., Gal-Yam, A., et al. 2021, *ApJL*, 907, L18
 De, K., Kasliwal, M. M., Cantwell, T., et al. 2018, *ApJ*, 866, 72
 De, K., Kasliwal, M. M., Tzanidakis, A., et al. 2020, *ApJ*, 905, 58
 de Vaucouleurs, G. H., de Vaucouleurs, A., & Shapley, H. 1964, Reference Catalogue of Bright Galaxies (Berlin: Springer)
 Denicoló, G., Terlevich, R., Terlevich, E., Forbes, D. A., & Terlevich, A. 2005, *MNRAS*, 358, 813
 Dessart, L., & Hillier, D. J. 2015, *MNRAS*, 447, 1370
 Dey, A., Schlegel, D. J., Lang, D., et al. 2019, *AJ*, 157, 168
 Draine, B. T., & Li, A. 2007, *ApJ*, 657, 810
 Eldridge, J. J., Stanway, E. R., Xiao, L., et al. 2017, *PASA*, 34, e058
 Flewelling, H. 2018, AAS Meeting Abstracts, 231, 436.01
 Foley, R. J. 2015, *MNRAS*, 452, 2463
 Fontana, A., Santini, P., Grazian, A., et al. 2009, *A&A*, 501, 15

- Foreman-Mackey, D., Sick, J., & Johnson, B. 2014, Python-Fsps: Python Bindings To Fsps, v0.1.1, Zenodo, doi:[10.5281/zenodo.12157](https://doi.org/10.5281/zenodo.12157)
- Frohmaier, C., Sullivan, M., Maguire, K., & Nugent, P. 2018, *ApJ*, **858**, 50
- Galbany, L., Ashall, C., Höflich, P., et al. 2019, *A&A*, **630**, A76
- Gallazzi, A., Charlot, S., Brinchmann, J., White, S. D. M., & Tremonti, C. A. 2005, *MNRAS*, **362**, 41
- Graur, O., Rodney, S. A., Maoz, D., et al. 2014, *ApJ*, **783**, 28
- Hinshaw, G., Larson, D., Komatsu, E., et al. 2013, *ApJS*, **208**, 19
- Jacobson-Galán, W. V., Margutti, R., Kilpatrick, C. D., et al. 2020a, *ApJ*, **898**, 166
- Jacobson-Galán, W. V., Margutti, R., Kilpatrick, C. D., et al. 2021, *ApJL*, **908**, L32
- Jacobson-Galán, W. V., Polin, A., Foley, R. J., et al. 2020b, *ApJ*, **896**, 165
- Jarrett, T. H., Chester, T., Cutri, R., Schneider, S. E., & Huchra, J. P. 2003, *AJ*, **125**, 525
- Johnson, B. D., Leja, J., Conroy, C., & Speagle, J. S. 2021, *ApJS*, **254**, 22
- Joye, W. A., & Mandel, E. 2003, in ASP Conf. Ser. 295, Astronomical Data Analysis Software and Systems XII, ed. H. E. Payne, R. I. Jedrzejewski, & R. N. Hook (San Francisco, CA: ASP), 489
- Kasliwal, M. M., Kulkarni, S. R., Gal-Yam, A., et al. 2012, *ApJ*, **755**, 161
- Kawabata, K. S., Maeda, K., Nomoto, K., et al. 2010, *Natur*, **465**, 326
- Kobayashi, C., Springel, V., & White, S. D. M. 2007, *MNRAS*, **376**, 1465
- Lang, D., Hogg, D. W., & Mykytyn, D. 2016, The Tractor: Probabilistic Astronomical Source Detection and Measurement, Astrophysics Source Code Library, ascl:[1604.008](https://ascl.net/1604.008)
- Lee, M. G., Jang, I. S., & Kang, J. 2019, *ApJ*, **871**, 33
- Leja, J., Carnall, A. C., Johnson, B. D., Conroy, C., & Speagle, J. S. 2019a, *ApJ*, **876**, 3
- Leja, J., Johnson, B. D., Conroy, C., Dokkum, P. G. v., & Byler, N. 2017, *ApJ*, **837**, 170
- Leja, J., Johnson, B. D., Conroy, C., et al. 2019b, *ApJ*, **877**, 140
- Leroy, A. K., Sandstrom, K. M., Lang, D., et al. 2019, *ApJS*, **244**, 24
- López Fernández, R., Cid Fernandes, R., González Delgado, R. M., et al. 2016, *MNRAS*, **458**, 184
- Lower, S., Narayanan, D., Leja, J., et al. 2020, *ApJ*, **904**, 33
- Lunnan, R., Kasliwal, M. M., Cao, Y., et al. 2017, *ApJ*, **836**, 60
- Lyman, J. D., Levan, A. J., Church, R. P., Davies, M. B., & Tanvir, N. R. 2014, *MNRAS*, **444**, 2157
- Lyman, J. D., Levan, A. J., James, P. A., et al. 2016, *MNRAS*, **458**, 1768
- MacLeod, M., Goldstein, J., Ramirez-Ruiz, E., Guillochon, J., & Samsing, J. 2014, *ApJ*, **794**, 9
- Makarov, D., Prugniel, P., Terekhova, N., Courtois, H., & Vauglin, I. 2014a, *A&A*, **570**, A13
- Makarov, D., Prugniel, P., Terekhova, N., Courtois, H., & Vauglin, I. 2014b, *A&A*, **570**, A13
- Maoz, D., & Badenes, C. 2010, *MNRAS*, **407**, 1314
- Maoz, D., & Graur, O. 2017, *ApJ*, **848**, 25
- Maoz, D., & Mannucci, F. 2012, *PASA*, **29**, 447
- Maoz, D., Mannucci, F., & Brandt, T. D. 2012, *MNRAS*, **426**, 3282
- Maoz, D., Mannucci, F., Li, W., et al. 2011, *MNRAS*, **412**, 1508
- Maoz, D., Mannucci, F., & Nelemans, G. 2014, *ARA&A*, **52**, 107
- Maoz, D., & Sharon, K. 2010, *ApJ*, **722**, 1879
- Margalit, B., & Metzger, B. D. 2016, *MNRAS*, **461**, 1154
- Martin, D. C., Fanson, J., Schiminovich, D., et al. 2005, *ApJL*, **619**, L1
- Mennekens, N., Vanbeveren, D., De Greve, J. P., & De Donder, E. 2010, *A&A*, **515**, A89
- Metzger, B. D. 2012, *MNRAS*, **419**, 827
- Milislavljevic, D., Patnaude, D. J., Raymond, J. C., et al. 2017, *ApJ*, **846**, 50
- Mitchell, P. D., Lacey, C. G., Baugh, C. M., & Cole, S. 2013, *MNRAS*, **435**, 87
- Mulchaey, J. S., Kasliwal, M. M., & Kollmeier, J. A. 2014, *ApJL*, **780**, L34
- Nakaoka, T., Maeda, K., Yamanaka, M., et al. 2021, *ApJ*, **912**, 30
- Nugent, A. E., Fong, W., Dong, Y., et al. 2020, *ApJ*, **904**, 52
- Oevirk, P., Pichon, C., Lançon, A., & Thiébaud, E. 2006, *MNRAS*, **365**, 46
- Pacifici, C., da Cunha, E., Charlot, S., et al. 2015, *MNRAS*, **447**, 786
- Patrel, G., Petit, C., Prugniel, P., et al. 2003a, *A&A*, **412**, 45
- Patrel, G., Theureau, G., Bottinelli, L., et al. 2003b, *A&A*, **412**, 57
- Perets, H. B., & Beniamini, P. 2021, *MNRAS*, **503**, 5997
- Perets, H. B., Gal-Yam, A., Mazzali, P. A., et al. 2010, *Natur*, **465**, 322
- Polin, A., Nugent, P., & Kasen, D. 2021, *ApJ*, **906**, 65
- Rosswog, S., Ramirez-Ruiz, E., & Hix, W. R. 2008, *ApJ*, **679**, 1385
- Salpeter, E. E. 1955, *ApJ*, **121**, 161
- Sandage, A. 1986, *A&A*, **161**, 89
- Sarbadhicary, S. K., Heiger, M., Badenes, C., et al. 2021, *ApJ*, **912**, 140
- Schlegel, D. J., Finkbeiner, D. P., & Davis, M. 1998, *ApJ*, **500**, 525
- Schulze, S., Yaron, O., Sollerman, J., et al. 2021, *ApJS*, **255**, 29
- Sebastian, B., Kharb, P., O'Dea, C. P., Gallimore, J. F., & Baum, S. A. 2019, *MNRAS*, **490**, L26
- Sell, P. H., Arur, K., Maccarone, T. J., et al. 2018, *MNRAS*, **475**, L111
- Sell, P. H., Maccarone, T. J., Kotak, R., Knigge, C., & Sand, D. J. 2015, *MNRAS*, **450**, 4198
- Shen, K. J., & Bildsten, L. 2009, *ApJ*, **699**, 1365
- Shen, K. J., Quataert, E., & Pakmor, R. 2019, *ApJ*, **887**, 180
- Simha, V., Weinberg, D. H., Conroy, C., et al. 2014, arXiv:[1404.0402](https://arxiv.org/abs/1404.0402)
- Skrutskie, M. F., Cutri, R. M., Stiening, R., et al. 2006, *AJ*, **131**, 1163
- Speagle, J. S. 2020, *MNRAS*, **493**, 3132
- Sullivan, M., Kasliwal, M. M., Nugent, P. E., et al. 2011, *ApJ*, **732**, 118
- Taubenberger, S. 2017, in The Extremes of Thermonuclear Supernovae, ed. A. W. Alsabti & P. Murdin (New York: Springer International), 317
- Tauris, T. M., Langer, N., & Podsiadlowski, P. 2015, *MNRAS*, **451**, 2123
- Tonry, J. L., Stubbs, C. W., Lykke, K. R., et al. 2012, *ApJ*, **750**, 99
- Toonen, S., Nelemans, G., & Portegies Zwart, S. 2012, *A&A*, **546**, A70
- Totani, T., Morokuma, T., Oda, T., Doi, M., & Yasuda, N. 2008, *PASJ*, **60**, 1327
- Valenti, S., Yuan, F., Taubenberger, S., et al. 2014, *MNRAS*, **437**, 1519
- Woosley, S. E., & Kasen, D. 2011, *ApJ*, **734**, 38
- Wright, E. L., Eisenhardt, P. R. M., Mainzer, A. K., et al. 2010, *AJ*, **140**, 1868
- Wuyts, S., Förster Schreiber, N. M., Lutz, D., et al. 2011, *ApJ*, **738**, 106
- Yates, R. M., Kauffmann, G., & Guo, Q. 2012, *MNRAS*, **422**, 215
- Yuan, F., Kobayashi, C., Schmidt, B. P., et al. 2013, *MNRAS*, **432**, 1680
- Zapartas, E., de Mink, S. E., Izzard, R. G., et al. 2017, *A&A*, **601**, A29
- Zenati, Y., Toonen, S., & Perets, H. B. 2019, *MNRAS*, **482**, 1135
- Zhou, S., Li, C., Hao, C.-N., et al. 2021, *ApJ*, **916**, 38